Structured solvent on a split electron tail: A semiclassical theory of electrified metal-solution interfaces

Mengke Zhang,[1,2] Yanxia Chen,[1,†] Michael Eikerling,[2,3] and Jun Huang[2,3,*]

[1] *Hefei National Research Center for Physical Science at Microscale and Department of Chemical Physics, University of Science and Technology of China, 230026 Hefei, China*

[2] *Institute of Energy Technologies, IET-3: Theory and Computation of Energy Materials, Forschungszentrum Jülich GmbH, 52425 Jülich, Germany*

[3] *Theory of Electrocatalytic Interfaces, Faculty of Georesources and Materials Engineering, RWTH Aachen University, 52062 Aachen, Germany*

(Received 19 August 2024; revised 16 December 2024; accepted 7 January 2025; published 4 February 2025)

We develop a comprehensive semiclassical continuum theory of electronic response and structured solvents at electrified metal-solution interfaces. The approach combines an orbital-free density-functional theory of electrons on the metal side with a statistical field theory of a structured electrolyte solution within a grand canonical framework. The resulting grand potential of the entire electrical double layer (EDL) is a hybrid functional of particle density, including metal electrons and classical solution particles, electric potential, and solvent polarization, referred to as density-potential-polarization functional theory (DPPFT). The DPPFT captures major atomistic phenomena within the EDL, including electron spillover, spatially damped oscillations in solvent polarization and electric potential extending toward the bulk solution, and the layered structure of ions. Based on DPPFT, an EDL model for the Ag(110)-KPF_6 aqueous solution interface is parameterized using experimental data for the double-layer capacitance (C_{dl}). The calibrated model is employed to study the influence of electronic, ion, and solvent properties on EDL structure. C_{dl} profiles at different crystal faces and in various electrolyte solutions are rationalized by the model coherently. We reveal that intensified ion layering enhances the capacitance at the potential of zero charge and narrowed ionic peaks in the C_{dl} profile. Contrary to classical models, the DPPFT allows coions to have appreciable densities near the metal surface, with their magnitudes depending on the local solvent structure and the correlation strength between ions and solvent. All in all, the presented framework provides a holistic and computationally efficient approach for atomistic-level modeling of EDLs under constant-potential conditions.

DOI: 10.1103/PhysRevApplied.23.024009

I. INTRODUCTION

The physics of electrified interfaces is the basis for numerous research fields, including but not limited to electrochemistry [1–4], nanofluidics [5–7], biology [8,9], and geological science [10]. In a nutshell, when an electronic conductor, often a metal, is immersed into an ionic conductor, often an aqueous solution, electronic and ionic charges of the same magnitude but opposite sign assemble at the interface between the adjacent phases, forming an electrical double layer (EDL).

Understanding the interactions between electrons, ions, and solvent molecules within the EDL has been a topic of intense research for the past two centuries. Current textbook understanding is neatly condensed into the Gouy-Chapman-Stern-Grahame (GCSG) model [11,12], which describes the EDL as an inner compact layer and an outer diffuse layer. The inner layer is further divided into an inner Helmholtz plane of specifically adsorbed ions and an outer Helmholtz plane at the position of the closest nonspecifically adsorbed ions. Ion densities in the diffuse layer are determined by the interplay between electrostatic, thermal, and excluded volume forces. Important modifications introduced to the GCSG model include the excluded volume effects due to the finite sizes of solution particles [13–16], dielectric screening effects of solvent molecules that reduce the dielectric permittivity near the charged electrode surface [16–18], specific adsorptions of ions and solvent molecules [19,20], and short-range correlations between ions that become increasingly important in concentrated solutions [21,22]. The GCSG model is well

*Contact author: ju.huang@fz-juelich.de
†Contact author: yachen@ustc.edu.cn

corroborated for mercury-like metals [23–25], as well as for *sd* metals like Ag and Au [26–31]. Applicability of the GCSG model for Pt-type metals remains a much-debated topic [20,32–34].

The GCSG model and its variants are often criticized for the absence of two essential features of an EDL. The first one is the electronic response on the metal side, where electrons, as a natural consequence of their quantum nature, spillover several angstroms from the metal surface [35,36]. Addressing the effects of this electronic response, the jellium models developed in the 1980s allow us to understand the dependency of the inner layer capacitance on the nature of the metal [37–39]. Nowadays, Kohn-Sham density-functional theory (DFT)-based models provide a largely satisfactory description of these electronic effects. The second atomistic feature of an EDL is the structure of the solvent layers. The structured solvent leads to spatially damped oscillations in solvent polarization and electric potential extending toward the bulk solution, as well as the layered structure of ions, as observed in molecular simulations [40–42].

The structured solvent can be described by continuum theories of structured dielectrics [43]. To this end, Berthoumieux, Kornyshev, and colleagues employed the phenomenological theory based on the Landau-Ginzburg approach where the free energy of solvent interactions is formulated as a functional of solvent polarization [44–46]. In this theory, electric potential and solvent polarization are two coupled field variables of the electrolyte solution. The theory delineates oscillations in electric potential and solvent polarization, alongside the layered structure of ions [46]. Recently, Blossey and Podgornik have developed a continuum theory of structured dielectrics rooted in statistical field theory, in which they coupled the ion charge density with the solvent polarization, enabling the description of short-range correlations between ions and solvent molecules [43,47,48]. These works have described the electrolyte solution side in great detail, while treating the metal surface as a featureless boundary condition. As a result, additional assumptions are necessary to specify the boundary condition of the solvent polarization at the metal surface.

While the two key drawbacks of the GCSG model can be treated by Kohn-Sham DFT and continuum theories of structured dielectrics, a comprehensive continuum theory of electronic response and structured solvent for the entire EDL is, to the best of our knowledge, non-existent. This work addresses this gap by developing a computationally efficient grand canonical theory, eliminating the need for additional assumptions on solvent polarization at the metal surface. For this, we combine an orbital-free DFT treatment of an inhomogeneous electron gas on the metal side with a statistical field theory of a structured electrolyte solution, unified within a grand canonical framework. The grand potential of the whole EDL is obtained as a hybrid functional of particle density (including both quantum electrons and classical solution particles), electric potential, and solvent polarization, referred to as density-potential-polarization functional theory (DPPFT). Compared to the earlier density-potential functional theory [49–52], DPPFT incorporates the short-range correlations between solvent molecules and hydration forces between ions and molecules on the electrolyte solution side.

The DPPFT treats both the metal and the electrolyte solution sides at the same atomistic level. In contrast, classical liquid theories, such as that developed by Hedley *et al.* [46] or Blossey and Podgornik [48], neglect the metal electrons. Kohn-Sham DFT-based models hybridized with primitive solvation models [53,54] fall short in delineating the atomistic features of the structured solvent at charged metal surfaces. We note that Kohn-Sham DFT hybridized with the reference interaction site method [49,55] or with explicit consideration of the solvent via force-field-based molecular dynamics [56,57] can describe the structured solvent and metal electronic properties. However, the high computational cost of these methods with the Kohn-Sham DFT at the core limits their applications to small systems, usually less than 1000 atoms. Based on the orbital-free DFT, DPPFT provides a holistic and computationally efficient approach to modeling EDLs under more realistic conditions.

The structure of this paper is as follows: First, we present a detailed formulation for the grand potential of the EDL by integrating orbital-free DFT for the inhomogeneous electron gas with statistical field theory for the structured electrolyte solution within a grand canonical framework. Next, we perform a variational analysis on the grand potential, leading to a closed set of equations that includes differential equations for electron density, electric potential, and solvent polarization, as well as nonlinear equations for the density distributions of electrolyte solution components and for the modified Langevin polarization equation. The resulting DPPFT model is subsequently solved for a one-dimensional case and parameterized with experimental data of the double-layer capacitance (C_{dl}) at the Ag(110)-KPF_6 aqueous solution interface. Finally, the calibrated model is then employed to study the influence of electronic, ion, and solvent properties on EDL structure and capacitance.

II. THEORY DEVELOPMENT

The EDL at a given electrode potential is an open system where quantum mechanical electrons and classical particles in the solution can exchange with the bulk phases. That is to say, the EDL is a grand canonical ensemble, and its thermodynamics is governed by the grand potential. Given that the metal consists of cationic cores and electrons, and the electrolyte solution contains cations, anions, and solvent molecules (denoted by cc, e, c, a, s subscripts),

the grand potential Ω of the EDL is obtained by a Legendre transformation of its Helmholtz free energy F,

$$\Omega = F - \int_r \left(n_e \tilde{\mu}_e + \sum_{i=a,c,s} n_i \tilde{\mu}_i \right), \tag{1}$$

where $\tilde{\mu}_e$ and $\tilde{\mu}_i$ are electrochemical potentials of electrons and solution component i, and n_e and n_i represent their number densities. The subscript of the integral sign denotes the integral variable. r represents the spatial coordinates, and $\int_r$ is a short-hand notation for $\iiint dxdydz$.

The Helmholtz free energy of the EDL is composed of the following contributions [58,59]:

(1) F_Q, the chemical free energy of the inhomogeneous electron gas, which is quantum mechanical in nature and includes the kinetic energy and exchange-correlation energy of electrons;
(2) F_C, the free energy from classical interactions in both phases, including the electrostatic interactions within the EDL, as well as short-range correlations and excluded volume interactions between electrolyte solution particles;
(3) $F_\otimes$, the free energy arising from the short-range interactions between the metal and electrolyte solution particles.

As a consequence, we have

$$F = F_Q + F_C + F_\otimes. \tag{2}$$

In the remainder of this section, we first treat F_Q with orbital-free DFT for the metal electrons in Sec. II A, then F_C with statistical field theory of the electrolyte solution in Sec. II B, and finally $F_\otimes$ with Morse potential descriptions for short-range interactions between the metal and solution particles in Sec. II C. Combining these free energy terms into Eq. (1), we obtain the grand potential of the EDL as a functional of particle density, electric potential, and solvent polarization. When the EDL is under equilibrium, the grand potential is minimized. In other words, the variation of the grand potential with respect to each of its functional variables is zero in the equilibrium state of the EDL. Based on this principle, in Sec. II D, we derive a closed set of equations governing the equilibrium properties of the EDL, including differential equations for electron density, electric potential, and solvent polarization, as well as nonlinear equations for the density distributions of solution components and the modified Langevin polarization equation. In Sec. II E, we identify the boundary conditions for the corresponding differential equations and in Sec. II F, we solve them in a one-dimensional case.

A. The metal

Orbital-free DFT expresses the kinetic energy T_{ni} as an explicit functional of the electron density n_e, ∇n_e, $\nabla^2 n_e$, etc., instead of deriving it from orbitals as in Kohn-Sham DFT. Combining explicit functionals for the kinetic energy and exchange-correlation energy U_{XC}, F_Q is written as

$$F_Q = T_{ni}[n_e, \nabla n_e, \ldots] + U_{XC}[n_e, \nabla n_e, \ldots]. \tag{3}$$

The kinetic energy of electrons is described herein by Thomas–Fermi–von Weizsäcker theory [60–62], which extends the Thomas-Fermi theory by incorporating an additional gradient term to account for the inhomogeneities in the electron gas, i.e.,

$$T_{ni}[n_e] = \int_r e_{au} a_0^{-3} t_{TF} (1 + \theta_T s^2), \tag{4}$$

with the volumetric kinetic energy given by the Thomas-Fermi theory,

$$t_{TF} = \frac{3}{10} (3\pi^2)^{2/3} (n_e a_0^3)^{5/3},$$

the correction for the gradient term, $(1 + \theta_T s^2)$, and the reduced gradient term,

$$s = \frac{1}{2} (3\pi^2)^{-(1/3)} |\nabla n_e| (n_e)^{-(4/3)}.$$

θ_T is a coefficient for the contribution of the gradient term in the kinetic energy. $e_{au} a_0^{-3}$ is used to transform the expression from atomic units to SI units, with atomic energy

$$e_{au} = \frac{e_0^2}{4\pi\epsilon_0 a_0},$$

Bohr radius a_0, elementary charge e_0, and vacuum permittivity ϵ_0.

The exchange-correlation energy U_{XC} is the sum of an exchange part u_X and a correlation part u_C [63],

$$U_{XC} = \int_r (u_X + u_C). \tag{5}$$

The terms u_X and u_C are described using the Perdew-Burke-Ernzerhof (PBE) functional [64]. Specifically, u_X is formulated as

$$u_X = e_{au} a_0^{-3} u_X^0 (1 + \theta_X s^2), \tag{6}$$

with the volumetric exchange energy of a uniform electron gas,

$$u_X^0 = -\frac{3}{4} \left(\frac{3}{\pi} \right)^{1/3} (n_e a_0^3)^{4/3}.$$

θ_X is a coefficient for the contribution of the gradient term in the exchange energy. Similarly, u_C is given by

$$u_C = e_{au}a_0^{-3}(u_C^0 + (n_e a_0^3)\theta_C t^2), \tag{7}$$

with the reduced gradient term

$$t = \frac{1}{4}\left(\frac{3}{\pi}\right)^{-(1/6)} a_0^4 |\nabla n_e| (n_e a_0^3)^{-(7/6)}.$$

θ_C is a coefficient for the contribution of the gradient term in the correlation energy. u_C^0 is the volumetric correlation energy of a uniform electron gas, for which we use the interpolation scheme of Perdew and Kurth [63], $u_C^0 = -2a_1(1 + a_2 r_s)(n_e a_0^3)\ln(1/\xi + 1)$, with the term $\xi = 2a_1(a_3 r_s^{1/2} + a_4 r_s + a_5 r_s^{3/2} + a_6 r_s^2)$, the radius $r_s = (4\pi n_e a_0^3/3)^{-(1/3)}$, and the coefficients

$$a_1 = 0.0310907, a_2 = 0.2137, a_3 = 7.5957, a_4 = 3.5876,$$
$$a_5 = 1.6382, a_6 = 0.49294.$$

Three aspects regarding the description of metal electrons need to be noted. Firstly, if we consider all electrons in the metal, the pseudopotential for the cationic cores is no longer required. Secondly, the electrostatic potential energy of electrons (Hartree potential) and cationic cores (external potential) is included in F_C. Thirdly, the entropy of the electron gas can be implicitly considered in the parameters of electronic functionals, T_{ni} and U_{XC}, which are temperature dependent, as in Ref. [65].

B. The electrolyte solution

1. Statistical field theory of structured dielectrics

The solvent is structured due to short-range correlations between solvent molecules and with ions. This structured solvent exhibits a nonlocal dielectric response and is referred to as a structured dielectric within a continuum description. Blossey and Podgornik have developed a comprehensive field theory of structured dielectrics based on the Onsager-Dupuis approach [47,48]. In this section, we primarily follow their treatment of the electrolyte solution to derive its grand canonical partition function, noting any differences as they arise.

We consider an electrolyte solution containing a pair of monovalent ions. We first introduce four statistical fields, i.e., the charge density field of cations $\hat{\rho}_c$, the charge density field of anions $\hat{\rho}_a$, the polarization field $\hat{\mathbf{P}}$, and the overall charge density field $\hat{\rho}$. Their spatial distributions depend on the positions of cations r_c, anions r_a, solvent molecules r_s, and the orientations of solvent molecules $\mathbf{n}$,

$$\hat{\rho}_c = e_0 \sum_{N_c} \delta(r - r_c), \tag{8}$$

$$\hat{\rho}_a = -e_0 \sum_{N_a} \delta(r - r_a), \tag{9}$$

$$\hat{\mathbf{P}}(r) = p \sum_{N_s} \mathbf{n}\delta(r - r_s), \tag{10}$$

$$\hat{\rho}(r) = \hat{\rho}_c(r) + \hat{\rho}_a(r) + \nabla \cdot \hat{\mathbf{P}}(r) + \rho_{ex}(r), \tag{11}$$

where N_c, N_a are the number of cations and anions and the summations over them iterate over the positions of all ions. N_s is the number of solvent molecules, and the summation iterates over the positions and orientations of all solvent molecules. ρ_{ex} is the external charge beyond that of the electrolyte solution, including the charges of metal electrons and cationic cores. Contrary to the treatment of Blossey and Podgornik, which introduces a combined density field for cations and anions, we define separate charge density fields for cations and anions, [47] to be able to consider the differences in the properties of cations and anions. Moreover, ρ_{ex} allows us to incorporate the long-range electrostatic interactions with the metal electrons and cationic cores into the Helmholtz free energy of classical interactions. The short-range interactions between the metal and the electrolyte solution are empirically described using Morse potentials, as detailed in Sec. II C. We define p as the magnitude of the solvent dipole moment and $\mathbf{n}$ as the normal unit vector pointing from the center of the positive charge to the negative charge of a solvent molecule. In this definition, $\hat{\mathbf{P}}$ specifically refers to the orientational polarization of solvent molecules, with the corresponding bound charge (polarization charge) expressed as

$$\hat{\rho}_b(r) = \nabla \cdot \hat{\mathbf{P}}(r). \tag{12}$$

The classical interaction energy $\hat{H}$ can be expressed in terms of the fields introduced above, specifically including the electrostatic interaction energy $\hat{H}_{es}$, short-range correlation energy between solvent molecules $\hat{H}_{corr}$, and short-range correlation energy between ions and solvent molecules $\hat{H}_{sr}$, i.e.,

$$\hat{H}[\hat{\rho}_a,\ \hat{\rho}_c, \hat{\rho}, \hat{\mathbf{P}}] = \hat{H}_{es}[\hat{\rho}] + \hat{H}_{corr}[\hat{\mathbf{P}}] + \hat{H}_{sr}[\hat{\rho}_c, \hat{\rho}_a, \hat{\mathbf{P}}]. \tag{13}$$

$\hat{H}_{es}$ can be given by the standard Coulomb interaction form,

$$\hat{H}_{es}[\hat{\rho}] = \frac{1}{2}\int_{r,r'} \hat{\rho}(r) G(r, r') \hat{\rho}(r'), \tag{14}$$

where

$$G(r,r') = \frac{1}{4\pi\epsilon_\infty |r-r'|}$$

is the Coulomb interaction potential with its inverse operator being $G^{-1}(r,r') = -\epsilon_\infty \nabla^2 \delta(r-r')$. The dielectric permittivity ϵ_∞ accounts for the nonorientational polarizations of the medium, including electronic and ionic polarization, which respond much faster than orientational polarization. Thus, ϵ_∞ is referred to as the high-frequency dielectric permittivity here.

$\hat{H}_{\rm corr}$ can be described as the spatial coupling of the polarization field. When the corresponding coupling potential is expanded up to fourth order, $\hat{H}_{\rm corr}$ can be expressed as a quadratic functional of polarization field $\hat{\mathbf{P}}$, its gradient $\nabla\cdot\hat{\mathbf{P}}$, and its second order gradient $\nabla^2\hat{\mathbf{P}}$ [47,48],

$$\hat{H}_{\rm corr}[\hat{\mathbf{P}}] = \frac{1}{2\epsilon_0}\int_r (K_{\rm s}\hat{\mathbf{P}}^2 + K_\alpha(\nabla\cdot\hat{\mathbf{P}})^2 + K_\beta(\nabla^2\hat{\mathbf{P}})^2), \tag{15}$$

where $K_{\rm s}, K_\alpha$, and K_β are coefficients of expanded terms. $K_{\rm s}$ is dimensionless, while $K_\alpha^{1/2}$ and $K_\beta^{1/4}$ have the dimension of length. The $K_{\rm s}$ term contributes to the local dielectric response, while K_α and K_β terms contribute to the nonlocal dielectric response.

$\hat{H}_{\rm sr}$ accounts for the spatial coupling between the polarization field and the charge density of ions, giving rise to the so-called hydration force. To the lowest order, $\hat{H}_{\rm sr}$ is expressed as a functional of ionic density fields and the gradient of polarization field [47,48],

$$\hat{H}_{\rm sr}[\hat{\rho}_{\rm c},\hat{\rho}_{\rm a},\hat{\mathbf{P}}] = \alpha_{\rm c}\int_r \hat{\rho}_{\rm c}\nabla\cdot\hat{\mathbf{P}} + \alpha_{\rm a}\int_r \hat{\rho}_{\rm a}\nabla\cdot\hat{\mathbf{P}}, \tag{16}$$

where $\alpha_{\rm c}, \alpha_{\rm a}$ are two coefficients that characterize the strength of short-range correlations between solvent and cations and between solvent and anions, respectively. In the classical interaction energy, the total solvation energy $\hat{H}_{\rm sol}$, arising from both the electrostatic and short-range correlation interactions, is given by,

$$\begin{aligned}\hat{H}_{\rm sol}[\hat{\rho}_{\rm c},\hat{\rho}_{\rm a},\hat{\mathbf{P}}] = &\int_r \hat{\rho}_{\rm c}(r)\left(\alpha_{\rm c} + \int_{r'} G(r,r')\right)\nabla\cdot\mathbf{P}(r') \\ &+ \int_{r'}\hat{\rho}_{\rm a}(r)\left(\alpha_{\rm c} + \int_r G(r,r')\right)\nabla\cdot\mathbf{P}(r').\end{aligned} \tag{17}$$

Since $G(r,r')$ is positive, negative values of $\alpha_{\rm c}$ and $\alpha_{\rm a}$ indicate that short-range correlations effectively reduce the impact of electrostatic interactions between ions and surrounding solvent molecules. This destabilizes the solvation structure governed by electrostatic interactions, resulting in a less negative solvation energy. Conversely, positive values of $\alpha_{\rm c}$ and $\alpha_{\rm a}$ effectively enhance electrostatic interactions between ions and surrounding solvent molecules, strengthen the solvation structure, and result in a more negative solvation energy.

Given the explicit form of the system Hamiltonian $\hat{H}$ in Eq. (13), the corresponding grand canonical partition function $Z_{\rm gc}$ is defined as

$$Z_{\rm gc}[T,\{\tilde{\mu}_i\}] = \sum_{N_{\rm s}}\sum_{N_{\rm c}}\sum_{N_{\rm a}} \lambda_{\rm s}^{N_{\rm s}}\lambda_{\rm c}^{N_{\rm c}}\lambda_{\rm a}^{N_{\rm a}} Z_{\rm c}, \tag{18}$$

with

$$\begin{aligned}Z_{\rm c}[T,\{N_i\}] = &\frac{1}{\Lambda_{\rm s}^{3N_{\rm s}}\Lambda_{\rm c}^{3N_{\rm c}}\Lambda_{\rm a}^{3N_{\rm a}}}\frac{1}{N_{\rm s}!N_{\rm c}!N_{\rm a}!} \\ &\int_{\mathbb{C}} \exp(-\beta\hat{H}[\hat{\rho}_{\rm c},\ \hat{\rho}_{\rm a},\hat{\rho},\hat{\mathbf{P}}]),\end{aligned} \tag{19}$$

where $\lambda_i = e^{\beta\tilde{\mu}_i}$ is the fugacity of solution component i, $\beta = 1/k_BT$ is the thermal constant, with Boltzmann constant k_B. The thermal de Broglie wavelength Λ_i ensures a dimensionless partition function. $Z_{\rm c}$ is the canonical partition function with temperature T and particle number $\{N_i\}$. The subscript $\mathbb{C}$ represents the integral measure over all configurational coordinates of particles, including their positions and the orientations of solvent molecules.

The field theoretical representation of the grand canonical partition function is derived following the same approach developed for anisotropic Coulomb fluids [66]. Given a functional $f(\hat{\varrho})$ of the field $\hat{\varrho}$, a collective field ϱ can be introduced using the sifting property of the Dirac delta functional $\delta(\varrho-\hat{\varrho})$, i.e.,

$$f(\hat{\varrho}) = \int_\varrho \delta(\varrho-\hat{\varrho}) f(\varrho). \tag{20}$$

In this way, we can introduce four collective fields $\rho_{\rm c},\ \rho_{\rm a},\ \rho,\ \mathbf{P}$ that respectively correspond to the previously defined fields $\hat{\rho}_{\rm c},\ \hat{\rho}_{\rm a},\ \rho,\ \hat{\mathbf{P}}$ in the integral kernel of $Z_{\rm c}$ in Eq. (19),

$$\begin{aligned}&\exp(-\beta\hat{H}[\hat{\rho}_{\rm c},\ \hat{\rho}_{\rm a},\hat{\rho},\hat{\mathbf{P}}]) \\ &= \int_{\rho_{\rm c}}\int_{\rho_{\rm a}}\int_{\mathbf{P}}\int_\rho \left(\prod_{\varrho=\rho_{\rm c},\rho_{\rm a},\rho,\mathbf{P}} \delta(\varrho-\hat{\varrho})\right) \\ &\quad\times \exp(-\beta H[\rho_{\rm c},\rho_{\rm a},\rho,\mathbf{P}]),\end{aligned} \tag{21}$$

with

$$H[\rho_c,\rho_a,\rho,\mathbf{P}] = \frac{1}{2}\int_{r,r'}\rho(r)G(r,r')\rho(r') + \frac{1}{2\epsilon_0}\int_r (K_s\mathbf{P}^2 + K_\alpha(\nabla\cdot\mathbf{P})^2 + K_\beta(\nabla^2\mathbf{P})^2) + \alpha_c\int_r \rho_c\nabla\cdot\mathbf{P} + \alpha_a\int_r\rho_a\nabla\cdot\mathbf{P}. \quad (22)$$

The collective fields are functions of spatial coordinates only. Further, the auxiliary field φ^* corresponding to the collective field ϱ in Eq. (21) can be introduced by the Fourier transform to ϱ in the Dirac delta functional $\delta(\varrho-\hat{\varrho})$ [67], i.e.,

$$\delta(\varrho-\hat{\varrho}) = \int_{\varphi^*}\exp\left(-i\int_r\beta\varphi^*(\varrho-\hat{\varrho})\right). \quad (23)$$

In this way, we introduce another four auxiliary fields ϕ_c^*, ϕ_a^*, ϕ^*, $\boldsymbol{\mathcal{E}}^*$ that correspond to the collective fields ρ_c, ρ_a, ρ, $\mathbf{P}$ in Eq. (21). The auxiliary fields are also functions of spatial coordinates only. By substituting Eq. (23) into Eq. (21), Z_c is reformulated as

$$Z_c = \frac{1}{\Lambda_s^{3N_s}\Lambda_c^{3N_c}\Lambda_a^{3N_a}}\frac{1}{N_s!N_c!N_a!}\times\int_{\mathbb{F}}\exp\left(-\beta\begin{pmatrix}H + i\int_r\boldsymbol{\mathcal{E}}^*\cdot\mathbf{P} + i\int_r\phi^*\rho\\ +i\int_r\phi_c^*\rho_c + i\int_r\phi_a^*\rho_a\end{pmatrix}\right)Z_c^0, \quad (24)$$

with

$$Z_c^0 = \int_{\mathbb{C}}\exp\left(i\beta\int_r(\boldsymbol{\mathcal{E}}^*\cdot\hat{\mathbf{P}} + \phi^*\hat{\rho} + \phi_c^*\hat{\rho}_c + \phi_a^*\hat{\rho}_a)\right), \quad (25)$$

where $\mathbb{F}$ denotes the integral measure over all collective fields and all auxiliary fields. Introduction of collective and auxiliary fields encapsulates the configurational coordinates into Z_c^0, whose exponential term can be directly evaluated as

$$\begin{aligned} &i\beta\int_r(\phi^*\hat{\rho} + \phi_c^*\hat{\rho}_c + \phi_a^*\hat{\rho}_a + \boldsymbol{\mathcal{E}}^*\cdot\hat{\mathbf{P}})\\ &= i\beta\int_r\phi^*\left(e_0\sum_{N_c}\delta(r-r_c) - e_0\sum_{N_a}\delta(r-r_a) + p\sum_{N_s}\mathbf{n}\cdot\nabla\delta(r-r_s) + \rho_{ex}(r)\right)\\ &+ i\beta e_0\int_r\phi_c^*\sum_{N_c}\delta(r-r_c) - i\beta e_0\int_r\phi_a^*\sum_{N_a}\delta(r-r_a)\\ &+ i\beta\int_r p\boldsymbol{\mathcal{E}}^*\cdot\sum_{N_s}\mathbf{n}\delta(r-r_s)\\ &= i\beta p\sum_{N_s}\mathbf{n}\cdot(\boldsymbol{\mathcal{E}}^*(r_s) - \nabla\phi^*(r_s))\\ &+ i\beta e_0\sum_{N_c}(\phi^*(r_c) + \phi_c^*(r_c))\\ &- i\beta e_0\sum_{N_a}(\phi^*(r_a) + \phi_a^*(r_a)) + i\beta\int_r\phi^*\rho_{ex}, \end{aligned} \quad (26)$$

where the first equality is obtained by recalling the definition of fields in Eqs. (8)–(11), and the second equality utilizes the sifting property of the Dirac delta function. Substituting Eq. (26) into Eq. (25), Z_c^0 can be integrated as

$$\begin{aligned} Z_c^0 = &\left(\int_r\exp(i\beta e_0\phi^* + i\beta e_0\phi_c^*)\right)^{N_c}\\ &\times\left(\int_r\exp(-i\beta e_0\phi^* - i\beta e_0\phi_a^*)\right)^{N_a}\\ &\times\left(\int_r d\mathbf{n}\exp(i\beta p\mathbf{n}\cdot(\boldsymbol{\mathcal{E}}^* - \nabla\phi^*))\right)^{N_s}\\ &\times\exp\left(i\beta\int_r\phi^*\rho_{ex}\right). \end{aligned} \quad (27)$$

The integration over $\mathbf{n}$ for solvent molecules can be made straightforward by going to spherical coordinates, i.e.,

$$\begin{aligned} &\int d\mathbf{n}\exp(i\beta p\mathbf{n}\cdot(\boldsymbol{\mathcal{E}}^* - \nabla\phi^*))\\ &= \frac{1}{4\pi}\int_0^\pi d\theta\,\sin\theta\int_0^{2\pi}d\varphi\exp(i\beta p\,\cos\theta|\boldsymbol{\mathcal{E}}^* - \nabla\phi^*|)\\ &= \frac{\sin(\beta p|\boldsymbol{\mathcal{E}}^* - \nabla\phi^*|)}{\beta p|\boldsymbol{\mathcal{E}}^* - \nabla\phi^*|}, \end{aligned} \quad (28)$$

where θ is the angle between $\mathbf{n}$ and the z axis, and φ is the polar angle. By substituting Eqs. (27) and (28) into Eq. (24), Z_{gc} is rearranged as follows,

$$Z_{gc} = \int_{\mathbb{F}}\exp\left(-\beta\left(H + i\int_r\boldsymbol{\mathcal{E}}^*\cdot\mathbf{P} + i\int_r\phi^*\rho + i\int_r\phi_c^*\rho_c + i\int_r\phi_a^*\rho_a - i\int_r\phi^*\rho_{ex}\right)\right)W, \quad (29)$$

with the series function,

$$W = \sum_{N_s}\sum_{N_c}\sum_{N_a} \frac{1}{N_s!N_c!N_a!}\left(\frac{\lambda_c}{\Lambda_c^3}\int_r \exp(i\beta e_0\phi^* + i\beta e_0\phi_c^*)\right)^{N_c} \times \left(\frac{\lambda_a}{\Lambda_a^3}\int_r \exp(-i\beta e_0\phi^* - i\beta e_0\phi_a^*)\right)^{N_a} \times \left(\frac{\lambda_s}{\Lambda_s^3}\frac{\sin(\beta p|\boldsymbol{\mathcal{E}}^* - \nabla\phi^*|)}{\beta p|\boldsymbol{\mathcal{E}}^* - \nabla\phi^*|}\right)^{N_s}. \tag{30}$$

It can be observed that W is exactly the series expansion of an exponential function, i.e.,

$$W = \exp\left(\frac{\lambda_c}{\Lambda_c^3}\int_r \exp(i\beta e_0\phi^* + i\beta e_0\phi_c^*)\right) \times \exp\left(\frac{\lambda_a}{\Lambda_a^3}\int_r \exp(-i\beta e_0\phi^* - i\beta e_0\phi_a^*)\right) \times \exp\left(\frac{\lambda_s}{\Lambda_s^3}\int_r \frac{\sin(\beta p|\boldsymbol{\mathcal{E}}^* - \nabla\phi^*|)}{\beta p|\boldsymbol{\mathcal{E}}^* - \nabla\phi^*|}\right). \tag{31}$$

Substituting Eq. (31) into Eq. (29) yields

$$Z_{gc} = \int_{\mathbb{F}} \exp\left(-\beta\left(H + i\int_r \boldsymbol{\mathcal{E}}^*\cdot\mathbf{P} + i\int_r \phi^*\rho + i\int_r \phi_c^*\rho_c + i\int_r \phi_a^*\rho_a - i\int_r \phi^*\rho_{ex} - V\right)\right), \tag{32}$$

with

$$V = \frac{1}{\beta}\int_r\left(\frac{\lambda_c}{\Lambda_c^3}\exp(i\beta e_0\phi^* + i\beta e_0\phi_c^*) + \frac{\lambda_a}{\Lambda_a^3}\exp(-i\beta e_0\phi^* - i\beta e_0\phi_a^*) + \frac{\lambda_s}{\Lambda_s^3}\frac{\sin(\beta p|\boldsymbol{\mathcal{E}}^* - \nabla\phi^*|)}{\beta p|\boldsymbol{\mathcal{E}}^* - \nabla\phi^*|}\right). \tag{33}$$

Now we obtain the field theoretical representation of the grand canonical partition function.

2. Saddle-point approximation

In this section, we simplify the functional integral in Eq. (32) using the saddle-point approximation. It is based on the idea that the dominant contributions to the functional integral come from the regions around the extrema (so-called saddle points) of the action in the exponential term of Eq. (32). At the saddle point, the auxiliary fields are purely imaginary, i.e., $\boldsymbol{\mathcal{E}}^* = i\boldsymbol{\mathcal{E}}$, $\phi^* = i\phi$, $\phi_c^* = i\phi_c$, $\phi_a^* = i\phi_a$, with $\boldsymbol{\mathcal{E}}, \phi, \phi_c, \phi_a$ being real-valued quantities [47]. In this scenario, fluctuations of the action around the saddle point are disregarded, corresponding to a mean-field level description. Fluctuations can be treated using the one-loop expansion, as in our previous work [50]. By substituting the auxiliary fields in Eq. (32) with corresponding real-valued quantities, we have

$$Z_{gc} \approx \exp\left(-\beta\left(H - \int_r \boldsymbol{\mathcal{E}}\cdot\mathbf{P} - \int_r \phi\rho - \int_r \phi_a\rho_a - \int_r \phi_c\rho_c + \int_r \phi\rho_{ex} - V\right)\right) \tag{34}$$

with

$$V = \frac{1}{\beta}\int_r\left(\frac{\lambda_c}{\Lambda_c^3}\exp(-\beta e_0\phi - \beta e_0\phi_c) + \frac{\lambda_a}{\Lambda_a^3}\exp(\beta e_0\phi + \beta e_0\phi_a) + \frac{\lambda_s}{\Lambda_s^3}\frac{\sinh(\beta p|\boldsymbol{\mathcal{E}} - \nabla\phi|)}{\beta p|\boldsymbol{\mathcal{E}} - \nabla\phi|}\right), \tag{35}$$

where we use the identity $\sin(ix) = i\sinh x$. In Eq. (34), we have omitted an integration constant that does not affect the results. The grand potential of the classical part Ω_C is directly derived from,

$$\Omega_C = -\frac{1}{\beta}\log Z_{gc} = H - \int_r \boldsymbol{\mathcal{E}}\cdot\mathbf{P} - \int_r \phi\rho - \int_r \phi_a\rho_a - \int_r \phi_c\rho_c + \int_r \phi\rho_{ex} - V. \tag{36}$$

To obtain F_C, we perform a Legendre transformation to convert the grand potential back into the Helmholtz free energy, i.e.,

$$F_C = \Omega_C + \sum_{i=a,c,s}\int_r n_i\tilde{\mu}_i^c, \tag{37}$$

where $\tilde{\mu}_i^c$ is the electrochemical potential of the solution component i in the classical part. The difference between $\tilde{\mu}_i^c$ and $\tilde{\mu}_i$ in Eq. (1) should be noted. The latter also accounts for short-range interactions between the metal and solution component i. The variables ρ_a and ρ_c in Eq. (36) are the charge densities of anions and cations, given by $\rho_a = -e_0 n_a$ and $\rho_c = e_0 n_c$. The particle number in the grand canonical ensemble is defined as $N_i = \int_r n_i = -(\partial\Omega_c/\partial\tilde{\mu}_i^c)$. By substituting Eq. (36) into this definition, we obtain

$$\tilde{\mu}_c^c = \frac{1}{\beta}\log(n_c\Lambda_c^3) + e_0(\phi + \phi_c), \tag{38}$$

$$\tilde{\mu}_a^c = \frac{1}{\beta}\log(n_a\Lambda_a^3) - e_0(\phi + \phi_a), \tag{39}$$

$$\tilde{\mu}_s^c = \frac{1}{\beta}\log(n_s\Lambda_s^3) - \frac{1}{\beta}\log\frac{\sinh(\beta p|\boldsymbol{\mathcal{E}} - \nabla\phi|)}{\beta p|\boldsymbol{\mathcal{E}} - \nabla\phi|}. \tag{40}$$

At equilibrium, Ω_C reaches its minimum value, with its variations with respect to ρ_c and ρ_a satisfying $\delta\Omega_C/\delta\rho_c =$

$\delta\Omega_C/\delta\rho_a = 0$. From this, we obtain

$$\phi_c = \alpha_c \nabla \cdot \mathbf{P}, \phi_a = \alpha_a \nabla \cdot \mathbf{P}. \tag{41}$$

Substituting Eqs. (36), (38)–(41) into Eq. (37), we obtain,

$$\begin{aligned} F_C = &\frac{1}{2}\int_{rr'} \rho(r)G(r,r')\rho(r') + \frac{1}{2\epsilon_0}\int_r (K_s\mathbf{P}^2 + K_\alpha(\nabla\cdot\mathbf{P})^2 \\ &+ K_\beta(\nabla^2\mathbf{P})^2) - \int_r \boldsymbol{\mathcal{E}}\cdot\mathbf{P} - \int_r \phi\rho + \int_r \phi\rho_{ex} \\ &+ \int_r n_c e_0(\phi + \alpha_c\nabla\cdot\mathbf{P}) - \int_r n_a e_0(\phi + \alpha_a\nabla\cdot\mathbf{P}) \\ &- \int_r \frac{n_s}{\beta}\log\frac{\sinh(\beta p|\boldsymbol{\mathcal{E}} - \nabla\phi|)}{\beta p|\boldsymbol{\mathcal{E}} - \nabla\phi|} \\ &+ \sum_{i=a,c,s}\int_r \frac{1}{\beta}(n_i\log(n_i\Lambda_i^3) - n_i). \end{aligned} \tag{42}$$

3. Excluded volume effects

In the above treatment, the excluded volume effects are not considered. To incorporate these effects, a volumetric excess free energy $\Phi_{ex}(\{n_i\})$ is often added into the Helmholtz free energy density f_C, defined as the kernel of the free energy functional $F_C = \int_r f_C$. Then the Helmholtz free energy density in Eq. (42) is modified to

$$\begin{aligned} f_C = &\frac{1}{2}\rho(r)G(r,r')\rho(r') + \frac{1}{2\epsilon_0}(K_s\mathbf{P}^2 + K_\alpha(\nabla\cdot\mathbf{P})^2 \\ &+ K_\beta(\nabla^2\mathbf{P})^2) - \boldsymbol{\mathcal{E}}\cdot\mathbf{P} - \phi\rho \\ &+ \phi\rho_{ex} + n_c e_0(\phi + \alpha_c\nabla\cdot\mathbf{P}) - n_a e_0(\phi + \alpha_a\nabla\cdot\mathbf{P}) \\ &- \frac{n_s}{\beta}\log\frac{\sinh(\beta p|\boldsymbol{\mathcal{E}} - \nabla\phi|)}{\beta p|\boldsymbol{\mathcal{E}} - \nabla\phi|} \\ &+ \sum_{i=a,c,s}\frac{1}{\beta}(n_i\log(n_i\Lambda_i^3) - n_i) + \Phi_{ex}(\{n_i\}). \end{aligned} \tag{43}$$

Budkov and Kolesnikov [68] and Lue [69] attempted to incorporate excluded volume effects self-consistently into the grand canonical partition function of the system. The excess chemical potential, defined as the derivative of the volumetric excess free energy with respect to particle density, can be expressed in a phenomenological manner based on previous studies by Bikerman [15], Eigen and Wicke [70,71], and Freise [72] that account for particle size effects,

$$\mu_i^{ex} = \frac{\partial\Phi_{ex}}{\partial n_i} = \frac{1}{\beta}\log\frac{1}{1 - \sum_{i=a,c,s} n_i\gamma_i\Lambda_B^3}, \tag{44}$$

where Λ_B is the characteristic length of reference lattice, with a maximum number density of referenced lattices, $n_{max} = \Lambda_B^{-3}$, and $\gamma_i = (2R_i)^3/\Lambda_B^3$ is the relative size of solution component i referenced to the size of lattice. R_i is the radius of electrolyte component i.

C. Short-range interactions between the metal and solution

The short-range interactions between the metal and solution particles mainly consist of chemical interactions and weak van der Waals interactions. While chemical interactions can be treated using the Newns-Anderson Hamiltonian for specific adsorptions [73,74] and van der Waals interactions using the Morse potential, here, we simply use the repulsive part of the Morse potential w_i to prevent solution particles from penetrating into the metal, i.e.,

$$F_\otimes = \sum_{i=a,c,s}\int_r n_i w_i, \tag{45}$$

with

$$w_i = D_i\exp(-2\beta_i(d - d_i)). \tag{46}$$

Here, D_i represents the depth of the Morse potential well, β_i is the coefficient controlling the width of the potential well, and d, d_i denote the distances from the position and the equilibrium position of electrolyte particle i to the metal surface, respectively. This simplified treatment is conceptually sufficient, as it effectively captures the strength of short-range interactions by tuning either the equilibrium distance or the well depth of the Morse potential. By combining Eqs. (3), (43), and (45) into Eq. (1), the grand potential density g, which is the kernel of the grand potential functional, i.e., $\Omega = \int_r g$, is obtained as follows:

$$\begin{aligned} g = &e_{au}a_0^{-3}t_{TF}(1 + \theta_T s^2) + e_{au}a_0^{-3}u_X^0(1 + \theta_X s^2) \\ &+ e_{au}a_0^{-3}(u_C^0 + (n_e a_0^3)\theta_C t^2) \\ &+ \frac{1}{2}\rho(r)G(r,r')\rho(r') + \frac{1}{2\epsilon_0}(K_s\mathbf{P}^2 + K_\alpha(\nabla\cdot\mathbf{P})^2 \\ &+ K_\beta(\nabla^2\mathbf{P})^2) - \boldsymbol{\mathcal{E}}\cdot\mathbf{P} - \phi\rho \\ &+ \phi\rho_{ex} + n_c e_0(\phi + \alpha_c\nabla\cdot\mathbf{P}) - n_a e_0(\phi + \alpha_a\nabla\cdot\mathbf{P}) \\ &- \frac{n_s}{\beta}\log\frac{\sinh(\beta p|\boldsymbol{\mathcal{E}} - \nabla\phi|)}{\beta p|\boldsymbol{\mathcal{E}} - \nabla\phi|} \\ &+ \sum_{i=a,c,s}\frac{1}{\beta}(n_i\log(n_i\Lambda_i^3) - n_i) + \Phi_{ex}(\{n_i\}) \\ &+ \sum_{i=a,c,s} n_i w_i - \left(n_e\tilde{\mu}_e + \sum_{i=a,c,s} n_i\tilde{\mu}_i\right), \end{aligned} \tag{47}$$

where g and Ω are the functionals of the field variables $\rho, \phi, \boldsymbol{\mathcal{E}}, \mathbf{P}$ and particle number density n_e, n_c, n_a, n_s.

D. Variational analysis on the grand potential

As previously mentioned, the variation of the grand potential with respect to each of its functional variables is

zero in the equilibrium state of the EDL, i.e.,

$$\frac{\delta\Omega}{\delta X} = 0 \ (X = \rho, \phi, \boldsymbol{\mathcal{E}}, \mathbf{P}, n_{\mathrm{e}}, n_{\mathrm{c}}, n_{\mathrm{a}}, n_{\mathrm{s}}). \tag{48}$$

For $X = n_{\mathrm{e}}$, Eq. (48) transforms into an Euler-Lagrange equation for n_{e}, i.e.,

$$\frac{\partial g}{\partial n_{\mathrm{e}}} - \nabla\left(\frac{\partial g}{\partial(\nabla n_{\mathrm{e}})}\right) = 0, \tag{49}$$

which gives

$$\begin{aligned}\bar{\nabla}\bar{\nabla}\bar{n}_{\mathrm{e}} = {} & \frac{20}{3}\bar{n}_{\mathrm{e}}\frac{\omega}{(\theta_T\omega - \theta_{\mathrm{XC}})} \\ & \times\left(\frac{\partial t_{\mathrm{TF}}}{\partial\bar{n}_{\mathrm{e}}} + \frac{\partial u_{\mathrm{X}}^0}{\partial\bar{n}_{\mathrm{e}}} + \frac{\partial u_{\mathrm{C}}^0}{\partial\bar{n}_{\mathrm{e}}} - \frac{(\tilde{\mu}_{\mathrm{e}} + e_0\phi)}{e_{\mathrm{au}}}\right) \\ & + \frac{\left(\theta_T\omega - \frac{4}{3}\theta_{\mathrm{XC}}\right)}{2\bar{n}_{\mathrm{e}}(\theta_T\omega - \theta_{\mathrm{XC}})}(\bar{\nabla}\bar{n}_{\mathrm{e}})^2,\end{aligned} \tag{50}$$

with dimensionless electron density $\bar{n}_{\mathrm{e}} = n_{\mathrm{e}}a_0^3$, dimensionless gradient operator $\bar{\nabla} = a_0\nabla$, the variable

$$\omega = \frac{2}{5}(3\pi^5)^{1/3}(\bar{n}_{\mathrm{e}})^{1/3},$$

and the constant $\theta_{\mathrm{XC}} = \theta_{\mathrm{X}} - (\pi^2/3)\theta_{\mathrm{C}}$. A detailed derivation was given in Ref. [58].

For $X = \rho$, Eq. (48) leads to

$$\phi = \int_{r'} G(r, r')\rho(r') = \int_{r'} \frac{\rho(r')}{4\pi\epsilon_\infty|r - r'|}, \tag{51}$$

i.e., the electric potential. Inversely, we obtain the Poisson equation

$$\rho = -\nabla(\epsilon_\infty\nabla\phi), \tag{52}$$

where ϵ_∞ varies spatially in the metal-solution interfacial region.

For $X = \boldsymbol{\mathcal{E}}$, Eq. (48) leads to the modified Langevin polarization equation,

$$\mathbf{P} = -\frac{pn_{\mathrm{s}}\mathcal{L}(\beta p|\boldsymbol{\mathcal{E}} - \nabla\phi|)}{|\boldsymbol{\mathcal{E}} - \nabla\phi|}(\boldsymbol{\mathcal{E}} - \nabla\phi), \tag{53}$$

where

$$\mathcal{L}(u) = \coth u - \frac{1}{u} = \frac{\partial\log(\sinh u/u)}{\partial u}$$

is the Langevin function.

For $X = \phi$, Eq. (48) gives

$$\frac{\partial g}{\partial\phi} - \nabla\left(\frac{\partial g}{\partial(\nabla\phi)}\right) = 0, \tag{54}$$

which, combined with Eqs. (52) and (53), gives the modified Poisson-Boltzmann equation,

$$\nabla\cdot(\epsilon_\infty\nabla\phi + \mathbf{P}) = -(n_c - n_a)e_0 - \rho_{\mathrm{ex}}, \tag{55}$$

with external charge density $\rho_{\mathrm{ex}} = (n_{\mathrm{cc}} - n_{\mathrm{e}})e_0$, where n_{cc} is the background charge density contributed by metal cationic cores.

For $X = \mathbf{P}$, Eq. (48) is transformed to

$$\frac{\partial g}{\partial\mathbf{P}} - \nabla\left(\frac{\partial g}{\partial(\nabla\cdot\mathbf{P})}\right) + \nabla^2\left(\frac{\partial g}{\partial\nabla^2\mathbf{P}}\right) = 0, \tag{56}$$

which gives

$$\epsilon_0^{-1}(K_{\mathrm{s}}\mathbf{P} - K_\alpha\nabla^2\mathbf{P} + K_\beta\nabla^4\mathbf{P}) - \alpha_{\mathrm{c}}e_0\nabla n_{\mathrm{c}} + \alpha_{\mathrm{a}}e_0\nabla n_{\mathrm{a}} = \boldsymbol{\mathcal{E}}. \tag{57}$$

For $X = n_{\mathrm{c}}, n_{\mathrm{a}}, n_{\mathrm{s}}$, Eq. (48) gives the electrochemical potentials of ions and solvent,

$$\tilde{\mu}_{\mathrm{c}} = \frac{1}{\beta}\log\frac{n_{\mathrm{c}}\Lambda_{\mathrm{c}}^3}{1 - \sum_i n_i\gamma_i\Lambda_{\mathrm{B}}^3} + e_0(\phi + \alpha_{\mathrm{c}}\nabla\cdot\mathbf{P}) + w_{\mathrm{c}}, \tag{58}$$

$$\tilde{\mu}_{\mathrm{a}} = \frac{1}{\beta}\log\frac{n_{\mathrm{a}}\Lambda_{\mathrm{a}}^3}{1 - \sum_i n_i\gamma_i\Lambda_{\mathrm{B}}^3} - e_0(\phi + \alpha_{\mathrm{a}}\nabla\cdot\mathbf{P}) + w_{\mathrm{a}}, \tag{59}$$

$$\begin{aligned}\tilde{\mu}_{\mathrm{s}} = {} & \frac{1}{\beta}\log\frac{n_{\mathrm{s}}\Lambda_{\mathrm{s}}^3}{1 - \sum_i n_i\gamma_i\Lambda_{\mathrm{B}}^3} \\ & - \frac{1}{\beta}\log\frac{\sinh(\beta p|\boldsymbol{\mathcal{E}} - \nabla\phi|)}{\beta p|\boldsymbol{\mathcal{E}} - \nabla\phi|} + w_{\mathrm{s}}.\end{aligned} \tag{60}$$

The physical significance of the introduced auxiliary fields at the mean-field level can be understood from Eqs. (58)–(60). Specifically, $\phi_{\mathrm{c}} = \alpha_{\mathrm{c}}\nabla\cdot\mathbf{P}$ and $\phi_{\mathrm{a}} = \alpha_{\mathrm{a}}\nabla\cdot\mathbf{P}$ are the effective potentials that embody the averaged effects of the short-range hydration forces on the cations and anions, respectively. $\boldsymbol{\mathcal{E}}$ is an average field that captures the averaged effect of the short-range correlations on the solvent molecule. These auxiliary fields vanish in the solution bulk due to its homogeneity and isotropy. At equilibrium, $\tilde{\mu}_i$ remains constant in the electrolyte solution,

which leads to the distributions of solution component i,

$$n_i = n_{\max}\frac{\chi_i\Theta_i}{1+\sum_i \gamma_i\chi_i(\Theta_i-1)}, \tag{61}$$

with the thermodynamic factor Θ_i

$$\Theta_c = \exp(-\beta e_0(\phi+\alpha_c\nabla\cdot\mathbf{P})-\beta w_c), \tag{62}$$

$$\Theta_a = \exp(\beta e_0(\phi+\alpha_a\nabla\cdot\mathbf{P})-\beta w_a), \tag{63}$$

$$\Theta_s = \frac{\sinh(\beta p|\boldsymbol{\mathcal{E}}-\nabla\phi|)}{\beta p|\boldsymbol{\mathcal{E}}-\nabla\phi|}\exp(-\beta w_s), \tag{64}$$

where the solution bulk is chosen as the reference for the electric potential. $\chi_i = n_i^b/n_{\max}$, where n_i^b is the bulk number density of solution component i.

Considering the possible presence of vacancies with number density n_v^b in the solution bulk, we have $\sum_i \gamma_i\chi_i + \chi_v = 1$ with $\chi_v = n_v^b/n_{\max}$. Equation (61) then becomes,

$$n_i = n_{\max}\frac{\chi_i\Theta_i}{\chi_v+\sum_i \gamma_i\chi_i\Theta_i}, \tag{65}$$

where

$$n_{\max} = \Lambda_B^{-3} = \left(\sum_i n_i^b\gamma_i\right)/(1-\chi_v).$$

We have arrived at a closed set of equations, comprising the differential equations for electron density [Eq. (50)], electric potential [Eq. (55)], and solvent polarization [Eq. (57)], along with the nonlinear equations for the density distributions of solution components [Eq. (65)] and the modified Langevin polarization equation [Eq. (53)]. These equations constitute the fundamental framework of the DPPFT model. When short-range correlations between solution particles are neglected, the auxiliary field $\boldsymbol{\mathcal{E}}$ in Eqs. (53) and (57) vanishes, and the present model reduces to the density-potential functional theory [58,73].

E. Boundary conditions

To solve the DPPFT model, it is essential to first determine the boundary conditions for the set of differential equations. We consider a metal-solution interface. The boundary conditions (BCs) in the distant solution bulk, that is, the right boundary conditions (RBCs) in the one-dimensional case, are

$$n_e = 0,\ \phi = 0,\ \mathbf{P} = 0,\ \nabla^2\mathbf{P} = 0, \tag{66}$$

where the first identity reflects the fact that metal electrons are absent in the solution bulk, the second identity defines the electric potential in the solution bulk as the potential reference, and the third identity means that solvent molecules are distributed homogenously and orientated isotropically in the solution bulk. The fourth identity serves as an additional boundary condition required for solving the fourth-order ordinary differential equation (ODE) in **P**. Here we choose the second-order gradient of the solvent polarization to be zero, as a consequence of the zero polarization charge in the solution bulk. This imposes a boundary condition for the variable introduced below for the reduction of the fourth-order ODE in **P**.

The BCs in the distant metal bulk, that is, the left boundary conditions (LBCs) in the one-dimensional case, are

$$\nabla n_e = 0,\ \nabla\phi = 0,\ \mathbf{P} = 0,\ \nabla^2\mathbf{P} = 0. \tag{67}$$

In the simplest scenario, the metal cationic cores are treated as a uniform background of positive charge density. In this case, the first and second equations imply that electron density and electric potential remain constant in the metal bulk, at sufficient distance from the interface. The distance to the left boundary from the metal surface should be large enough, say greater than 10 Å, to ensure accessibility to the metal bulk. For the case where size and arrangement of metal cationic cores are explicitly considered, we can take the boundary at the central plane of metal cationic cores. The third identity reflects the absence of solvent molecules in the metal phase, and then the fourth identity is obvious.

In this model, constant-potential conditions are implemented by varying the electrochemical potential $\tilde{\mu}_e$ in Eq. (50) [75]. The electrochemical potential of metal electrons is related to the chemical potential μ_e, and the inner potential of the metal ϕ_M by

$$\tilde{\mu}_e = -e_0\phi_M + \mu_e. \tag{68}$$

In numerical implementations, Eq. (53) can be treated as a zeroth-order differential equation in $\boldsymbol{\mathcal{E}}$. $\boldsymbol{\mathcal{E}}$ equals zero both in the metal bulk, where no solvent molecules are present, and in the solution bulk, due to isotropic short-range correlations.

F. Numerical implementation

In this section, we present the numerical implementation of the one-dimensional DPPFT model, which is suitable for homogenous metal surfaces, e.g., single-crystal surfaces. In the one-dimensional case, **P** and $\boldsymbol{\mathcal{E}}$ are reduced to scalar quantities, $P, \mathcal{E}$, with positive values indicating that the fields are directed toward the solution bulk. We define dimensionless variables, marked with an overbar,

as follows:

$$\bar{n}_i = {a_0}^3 n_i,\ \bar{x} = \frac{x}{a_0},\ \bar{\phi} = \frac{e_0\phi}{k_B T},\ \bar{p} = \frac{p}{e_0 a_0},\ \bar{\epsilon}_\infty = \frac{\epsilon_\infty}{\epsilon_0},$$
$$\bar{P} = \frac{\kappa a_0^2 P}{e_0},\ \bar{\mathcal{E}} = \frac{e_0 a_0 \mathcal{E}}{k_B T},\ \bar{K}_\alpha = \frac{K_\alpha}{a_0^2},\ \bar{K}_\beta = \frac{K_\beta}{a_0^4},$$
$$\bar{\alpha}_i = \frac{\epsilon_0 \alpha_i}{a_0^2},\ \bar{\beta}_i = \beta_i a_0, \tag{69}$$

where $\kappa = e_0^2/k_B T a_0 \epsilon_0$ is a constant. The modified Poisson-Boltzmann equation in Eq. (53) is rewritten in dimensionless variables as

$$\bar{\nabla}(\bar{\epsilon}_\infty \bar{\nabla}\bar{\phi} + \bar{P}) = -\kappa(\bar{n}_{cc} - \bar{n}_e + \bar{n}_c - \bar{n}_a), \tag{70}$$

where the dimensionless number densities of ions and solvent molecules are given as

$$\bar{n}_i = \bar{n}_{max}\frac{\chi_i \Theta_i}{\chi_v + \sum_{i=a,c,s}\gamma_i \chi_i \Theta_i} \tag{71}$$

with Θ_i expressed in dimensionless variables,

$$\Theta_c = \exp(-\bar{\phi} - \bar{\alpha}_c \bar{\nabla}\bar{P} - \beta w_c), \tag{72}$$
$$\Theta_a = \exp(\bar{\phi} + \bar{\alpha}_a \bar{\nabla}\bar{P} - \beta w_a), \tag{73}$$
$$\Theta_s = \frac{\sinh(\bar{p}|\bar{\mathcal{E}} - \bar{\nabla}\bar{\phi}|)}{\bar{p}|\bar{\mathcal{E}} - \bar{\nabla}\bar{\phi}|}\exp(-\beta w_s). \tag{74}$$

By introducing the second-order derivative field $\mathbf{Q} = \nabla^2\mathbf{P}$, the fourth-order ODE [Eq. (57)] is decomposed into two second-order ODEs in $\mathbf{Q}$ and in $\mathbf{P}$. In their dimensionless form, they are written as follows:

$$K_s\bar{P} - \bar{K}_\alpha\bar{Q} + \bar{K}_\beta\bar{\nabla}^2\bar{Q} - \kappa\bar{\alpha}_c\bar{\nabla}\bar{n}_c + \kappa\bar{\alpha}_a\bar{\nabla}\bar{n}_a = \bar{\mathcal{E}}, \tag{75}$$

$$\bar{\nabla}^2\bar{P} = \bar{Q}, \tag{76}$$

where $\bar{Q} = (\kappa a_0^4/e_0)Q$ is the dimensionless derivative field. Equations (66) and (67) impose the LBC and RBC for Eq. (75), i.e., $\bar{Q} = 0$ at both boundaries. The modified Langevin polarization equation can be rewritten in dimensionless variables as

$$\bar{P} = -\frac{\kappa\bar{p}\bar{n}_s\mathcal{L}(\bar{p}|\bar{\mathcal{E}} - \bar{\nabla}\bar{\phi}|)}{|\bar{\mathcal{E}} - \bar{\nabla}\bar{\phi}|}(\bar{\mathcal{E}} - \bar{\nabla}\bar{\phi}). \tag{77}$$

We substitute $\psi = (\bar{n}_e)^{1/3}$ to get rid of fractional exponents of $\bar{n}_e$ [58]. In this scheme, Eq. (50) can then be rewritten as

$$\bar{\nabla}\bar{\nabla}\psi + \frac{\theta_T\omega}{2(\theta_T\omega - \theta_{XC})\psi}(\bar{\nabla}\psi)^2 = \frac{20}{9}\psi\frac{\omega}{(\theta_T\omega - \theta_{XC})} \times\left(\frac{\partial t_{TF}}{\partial\bar{n}_e} + \frac{\partial u_X^0}{\partial\bar{n}_e} + \frac{\partial u_C^0}{\partial\bar{n}_e} - \frac{(\tilde{\mu}_e + e\phi)}{e_{au}}\right). \tag{78}$$

Equations (70) and (75)–(78) are solved in COMSOL. Technical details on the numerical implementation are provided in the Supplemental Material [76]. The present model can be extended to nonmetallic electrodes with a modified treatment of the electronic structure. For instance, semiconducting electrodes can also be described using orbital-free DFT with a band-gap-dependent kinetic energy functional, e.g., using the linear-response kernel of the jellium-with-gap model [77].

III. RESULTS AND DISCUSSIONS

A. Model parameterization and calibration

The model parameters for the base case are summarized in Tables I–III. Most parameters are obtained from the literature, while the remaining ones are calibrated by fitting experimental double-layer capacitance data for the Ag(110)-KPF_6 aqueous solution interface [28], as noted in the tables. The weak specific adsorption of ions at this interface removes the need for further consideration.

Metal cationic cores, in the simplest case, are described as a uniform charge background with a dimensionless positive charge density $\bar{n}_{cc}^0$, namely,

$$\bar{n}_{cc} = \bar{n}_{cc}^0\theta(\bar{x}_M - \bar{x}), \tag{79}$$

where $\theta(x)$ is the Heaviside step function, with $\bar{x}_M$ denoting the dimensionless position of the metal surface, and

$$n_{cc}^0 = 4N_{Ag}\left(\frac{a_0}{a_{Ag}}\right)^3 = 0.408,$$

with $N_{Ag} = 47$ representing the number of electrons of a silver atom. Moreover, $a_{Ag} = 4.086$ Å is the length of the cubic close-packed cell of silver, which contains four silver atoms. Considering all electrons, ϵ_0 is used as the high-frequency dielectric permittivity of the metal, namely, $\bar{\epsilon}_{\infty,M} = 1$. We use the PBE functional with $\theta_X = 0.1235$ and $\theta_C = 0.0667$ [63]. The only free parameter in electronic functionals is the coefficient in the kinetic energy θ_T, which is calibrated according to the experimental potential of zero charge. The full-electron consideration is a simplified treatment that lumps interactions between electrons in different orbitals into a single parameter θ_T. This simple treatment is sufficient for our purpose because there is no formation or cleavage of chemical bonds at the considered interface. If one takes into account only the valence electrons of the metal, the pseudopotential and electronic polarization of the metal cationic cores should be taken into account [82,83].

On the solution side, we use $R_{sol} = 2.75$ Å as the diameter of water molecules [80], which serves as the reference size, i.e., $\Lambda_B = R_{sol}$. For K^+ cations, their solvation shell comprises a tightly bound first layer of water molecules and more loosely bound outer layers. Therefore, we treat

TABLE I. Metal parameters of the base case.

Symbol	Item	Value	Source
a_1	Coefficient in the PBE functional	0.0310907	Ref. [63]
a_2	Coefficient in the PBE functional	0.2137	Ref. [63]
a_3	Coefficient in the PBE functional	7.5957	Ref. [63]
a_4	Coefficient in the PBE functional	3.5876	Ref. [63]
a_5	Coefficient in the PBE functional	1.6382	Ref. [63]
a_6	Coefficient in the PBE functional	0.49294	Ref. [63]
θ_X	Gradient coefficient in the exchange functional	0.1235	Ref. [63]
θ_C	Gradient coefficient in the correlation functional	0.0667	Ref. [63]
θ_T	Gradient coefficient in the kinetic energy functional	1.585	Fitted to C_{dl}
$\epsilon_{\infty,M}$	High-frequency dielectric permittivity of the metal	ϵ_0	Ref. [58]
$\bar{n}^0_{cc}$	Dimensionless charge density of metal cationic cores	0.408	Ref. [58]

the cation with its first solvation layer as an integrated structure and introduce α_c to account for the short-range correlations between this tightly solvated cation and solvent molecules in outer layers. Molecular dynamics simulations have shown that the distance between K^+ and the oxygen atoms in its first solvation layer ranges from 2.6 to 3.6 Å [78], and we use the upper limit, 3.6 Å, as the radius of the tightly solvated cation. There is no such tightly solvated structure for the PF_6^- anions; therefore, their size is taken as the value of the bare anion. In this scenario, α_a accounts for the short-range correlations between the bare anion and the surrounding water molecules. The radius of solvated PF_6^- has been determined to range between 4 and 6 Å [79]. By subtracting the diameter of a water molecule, the effective radius of bare PF_6^- is approximately 2.7 Å. The fraction of vacancy lattice sites in the solution bulk can be calculated as $\chi_v = 1 - \Lambda_B^3 \sum_i n_i^b \gamma_i$, with $n_s^b = 55.6\ \mathrm{mol\,m^{-3}}$.

Under quasistatic conditions, as the frequency of the electric field approaches zero, the solvent polarization responds linearly to the electric field. This implies that in Eq. (53), $\boldsymbol{\mathcal{E}}$ is linear with $\mathbf{P}$. The linear relationship is given by Eq. (57), $\boldsymbol{\mathcal{E}} = \epsilon_0^{-1} K_s \mathbf{P}$. Substituting this relationship into Eq. (53) and considering the solution bulk, we obtain the static dielectric permittivity ϵ_s in the solution bulk,

$$\epsilon_s = \epsilon_{\infty,S} + \frac{\beta p^2 n_s^b}{3\epsilon_0 + \beta p^2 n_s^b K_s}\epsilon_0 = \epsilon_{\infty,S} + \frac{1}{3}\beta n_s^b p_{eff}^2 \quad (80)$$

with an effective dipole moment of

$$p_{eff} = \left(\frac{3(\epsilon_s - \epsilon_{\infty,S})}{\beta n_s^b}\right)^{1/2} = \left(1 + \frac{\beta p^2 n_s^b K_s}{3\epsilon_{\infty,S}}\right)^{-(1/2)} p. \quad (81)$$

For water, based on its dielectric dispersion spectrum [81], $\epsilon_{\infty,S}$ and ϵ_s are approximately 4.5 ϵ_0 and 78.5 ϵ_0, respectively. These values of dielectric permittivity lead to an effective dipole moment of 4.66 D as obtained from Eq. (81). This value is greater than the intrinsic dipole moment of 1.85 D for a water molecule, reflecting an enhanced dielectric screening capability of water molecules in solution. This is rationalized as a consequence of short-range correlations between solvent molecules, as incorporated in our present model and shown in Eq. (81). Another factor contributing to the greater effective dipole moment is the cavity field effect. Specifically, a water molecule experiences a stronger local electric field, called the cavity field, than the macroscopic electric field in the medium due to screening by the surrounding medium. This cavity field effect, as considered by Gongadze and Iglič [84], is expected to induce notable changes in the effective dipole moment at highly charged metal surfaces.

The continuous transition of the high-frequency dielectric constant near the metal surface is described as [58]:

$$\bar{\epsilon}_\infty(\bar{x}) = \bar{\epsilon}_{\infty,M} + \frac{\bar{\epsilon}_{\infty,S} - \bar{\epsilon}_{\infty,M}}{2}(1 - \mathrm{erf}(-\bar{\beta}_\infty(\bar{x} - \bar{x}_M))) \quad (82)$$

with the error function $\mathrm{erf}(\bar{x})$. $\bar{\beta}_\infty$ is a dimensionless coefficient controlling the width of the transition region, and we use the value of 1 inherited from Ref. [58].

In this study, the coefficients of short-range correlations, K_α, K_β, along with α_c, α_a, are calibrated using experimental C_{dl} data. As shown in Table II, the calibrated values of α_c and α_a are negative, suggesting that short-range correlations between ions and solvent molecules result in less negative solvation energies. The exclusion of short-range correlations between the ion and solvent molecules is one of the reasons for the solvation energy predicted by the Born model being more negative than the experimental value, especially for small ions. Another reason for this discrepancy is that the dielectric response of spatially correlated solvent molecules to the ionic charge reduces the effective dielectric permittivity near the ion, a phenomenon known as dielectric saturation [85], which is also accounted for in our model. From this perspective, our model can effectively address ion solvation, allowing

TABLE II. Solution parameters of the base case.

Symbol	Item	Value	Source
c_s^b	Bulk solvent concentration	55600 mol m^{-3}	Ref. [58]
R_c	Radius of tightly solvated cations	3.6 Å	Ref. [78]
R_a	Radius of bare anions	2.7 Å	Ref. [79]
R_{sol}	Diameter of solvent molecules	2.75 Å	Ref. [80]
$\epsilon_{\infty,S}$	High-frequency dielectric permittivity of the solution	4.53 ϵ_0	Ref. [81]
ϵ_s	Static dielectric permittivity in the solution bulk	78.5 ϵ_0	Ref. [81]
K_α	Coefficient in the short-range correlation functional of solvent molecules	$-0.35\ a_0^2$	fitted to C_{dl}
K_β	Coefficient in the short-range correlation functional of solvent molecules	$0.145\ a_0^4$	fitted to C_{dl}
α_c	Strength of short-range correlations between tightly solvated cations and water molecules	$-0.05\ a_0^2/\epsilon_0$	fitted to C_{dl}
α_a	Strength of short-range correlations between bare anions and water molecules	$-0.081\ a_0^2/\epsilon_0$	fitted to C_{dl}

for the calibration of α_c and α_a by the use of ion solvation energies. Additionally, the coefficients K_α and K_β can be determined by fitting the nonlocal dielectric response function of water from the model to the corresponding results from molecular simulations [44,46]. The detailed formalism of the nonlocal dielectric response function in our model and its comparison to simulation results will be presented in future studies.

Parameters of the Morse potentials used to describe the short-range interactions between the metal and solution particles can be acquired from Kohn-Sham DFT calculations [86]. In the present treatment, we use the repulsive part of the Morse potential to prevent solution particles from penetrating into the metal phase. In this case, Eq. (46) can be recast into the form

$$w_i = k_B T \exp(-2\beta_i(d - d_i^M)), \tag{83}$$

with

$$d_i^M = d_i + \frac{\ln(D_i/k_B T)}{2\beta_i}, \tag{84}$$

where d_i^M is the effective equilibrium distance of solution component i from the metal surface. The parameters D_i and d_i are combined into a single effective parameter d_i^M, where smaller values indicate that the solution component i can approach the metal surface more closely, corresponding to stronger short-range interactions with the metal surface. The values of d_i^M and β_i in Eq. (83) are calibrated to reproduce experimental C_{dl} data, as shown in Table III. The calibrated values of d_i^M capture the phenomenon that ions are positioned farther from the metal surface than water molecules.

As discussed above, $\theta_T, K_\alpha, K_\beta, \alpha_i, d_i^M$, and β_i are estimated by fitting C_{dl} profiles at three ion concentrations measured by Valette [28]. The impact of these parameters on the model results will be gauged in a parametric analysis in Sec. III C. In the C_{dl} is calculated by taking the derivative of the surface free charge σ_{free} with respect to ϕ_M,

$$C_{dl} = \frac{\partial \sigma_{free}}{\partial \phi_M} = -e_0 \frac{\partial \sigma_{free}}{\partial \tilde{\mu}_e} = \frac{e_0^2}{a_0^2} \frac{\partial}{\partial \tilde{\mu}_e} \int d\bar{x}(\bar{n}_c - \bar{n}_a)$$
$$= \frac{e_0^2}{a_0^2} \frac{\partial}{\partial \tilde{\mu}_e} \int d\bar{x}(\bar{n}_e - \bar{n}_{cc}), \tag{85}$$

with the surface free charge

$$\sigma_{free} = \frac{e_0}{a_0^2} \int d\bar{x}(\bar{n}_c - \bar{n}_a) = \frac{e_0}{a_0^2} \int d\bar{x}(\bar{n}_e - \bar{n}_{cc}).$$

The electrode potential measured in experiments [28], using the saturated calomel electrode (SCE) scale and denoted as E_{SCE}, can be converted to $\tilde{\mu}_e$ using

$$-\tilde{\mu}_e = e_0(E_{SCE} + E_{SHE}^* + 0.2415\ \text{V}) - e_0 \chi_s, \tag{86}$$

where 0.2415 V transforms the electrode potential from SCE scale to standard hydrogen electrode (SHE) scale. E_{SHE}^* is the absolute electrode potential of the SHE, for which we use the value of 4.44 V [87]. The last term arises from the consideration that we take the inner potential of the electrolyte solution as the potential [88]. χ_s is the surface potential of the solution-vacuum interface, and we adopt the recommended value of 0.17 V for the water-vacuum interface [87].

Figure 1 compares model-based and experimental C_{dl} data at the Ag(110)-KPF_6 aqueous solution interface for KPF_6 concentrations of 20, 40, and 100 mM. The electrode potential is referenced to the potential of zero charge (PZC), viz. position of the Gouy-Chapman minimum. At the Gouy-Chapman minimum, $\tilde{\mu}_e = -3.53$ eV, corresponding to a PZC of -0.98 V vs SCE. It is worth noting that the PZC is taken directly as an EDL parameter in classical models, while the present model derives it from an orbital-free description of metal electrons. Model results at three concentrations are calculated using the same set of model parameters in Tables I–III. The model reproduces well the camel shape of C_{dl} curves, as well as

TABLE III. Metal-solution interaction parameters of the base case, all fitted to C_{dl}.

Symbol	Item	Value
$\bar{\beta}_s$	Dimensionless coefficient in the Morse potential of solvent molecules	0.95
$\bar{\beta}_c$	Dimensionless coefficient in the Morse potential of cations	0.19
$\bar{\beta}_a$	Dimensionless coefficient in the Morse potential anions	4.5
d_s^M	Effective equilibrium distance of solvent molecules	6.6 a_0
d_c^M	Effective equilibrium distance of cations	13.3 a_0
d_a^M	Effective equilibrium distance of anions	11.6 a_0

the trend of the C_{dl} curve with concentration, namely the decrease in the Gouy-Chapman minimum and the larger distance between two camel peaks as the concentration decreases. The agreement between model and experiment is greatly improved compared to a previous work [58]. The improvement is discernable in the magnitude of C_{dl} and the distance between the two peaks in C_{dl} curves. The microscopic structure of the EDL behind the C_{dl} curves, as well as the influence of model parameters on the interfacial structure and consequently on the C_{dl} curves, will be discussed in Secs. III B and III C.

B. Interfacial structure

The model can delineate a spatially resolved atomistic-scale picture of the EDL. Toward a more realistic description of the metal-solution interface, we consider a one-dimensional discrete periodic arrangement of metal cationic cores. The charge distribution of metal cationic cores in this case is written as follows[73]:

$$\frac{\bar{n}_{cc}(x)}{\bar{n}_{cc}^0} = \theta(x) - \theta\left(x - \frac{a_{cc}}{2}\right) + \theta\left(x - \frac{a_{cc}}{2} - t\right) - \theta\left(x - \frac{3a_{cc}}{2} - t\right) + \theta\left(x - \frac{3a_{cc}}{2} - 2t\right) - \theta\left(x - \frac{5a_{cc}}{2} - t\right) + \theta\left(x - \frac{5a_{cc}}{2} - 3t\right) - \theta\left(x - \frac{7a_{cc}}{2} - 3t\right) + \theta\left(x - \frac{7a_{cc}}{2} - 4t\right) - \theta\left(x - \frac{9a_{cc}}{2} - 4t\right), \quad (87)$$

where x is the distance from the left boundary, a_{cc} the diameter of metal cationic cores, t the separation distance between two metal cationic cores, $\bar{n}_{cc}^0$ the dimensionless charge density of metal cationic cores. In this scheme, only valence electrons are considered, while core electrons are embedded into metal cationic cores. The electronic polarization of metal cationic cores results in a high-frequency dielectric permittivity larger than the vacuum permittivity. These parameters can be obtained using DFT calculations. Here, we use $a_{cc} = 1.1$ Å, $t = 1.25$ Å, $\bar{n}_{cc}^0 = 0.2042$, and $\bar{\epsilon}_{\infty,M} = 2$ as in Ref. [73]. Other parameters remain the same as in Tables I–III. Figures 2 and 3 present model results for the spatial distributions of electron density, solvent polarization, electric potential, and the number density of solution components at the Ag(110)-0.1 M KPF_6 aqueous solution interface. The results are shown for five electrode potentials relative to the PZC. In these plots, the metal edge is shifted to $x = 0$.

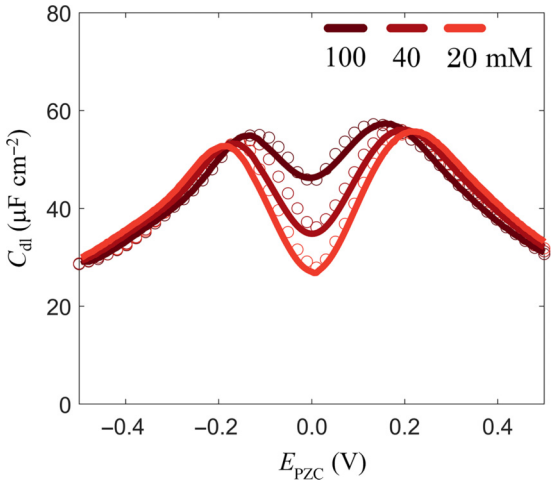

FIG. 1. Model (lines) and experimental results (circles) of the differential double-layer capacitance C_{dl} at the Ag(110)-KPF_6 aqueous solution interface for KPF_6 concentrations of 20, 40, and 100 mM, respectively. E_{PZC} is the electrode potential referenced to the potential of zero charge (PZC). The experimental data, measured by Valette, are corrected using a roughness factor of 1.15 as suggested [28]. The same set of parameters, as listed in Tables I–III, is used across all three concentrations.

1. Oscillation

In Fig. 2(a), due to the discreteness of metal cationic cores, the electron density and electric potential oscillate in the metal phase. The electrons spill out of the metal edge by approximately 2 Å, with the extent of this spillover increasing at more negative electrode potentials. This is because the electrochemical potential of electrons is more positive at more negative electrode potentials, enabling

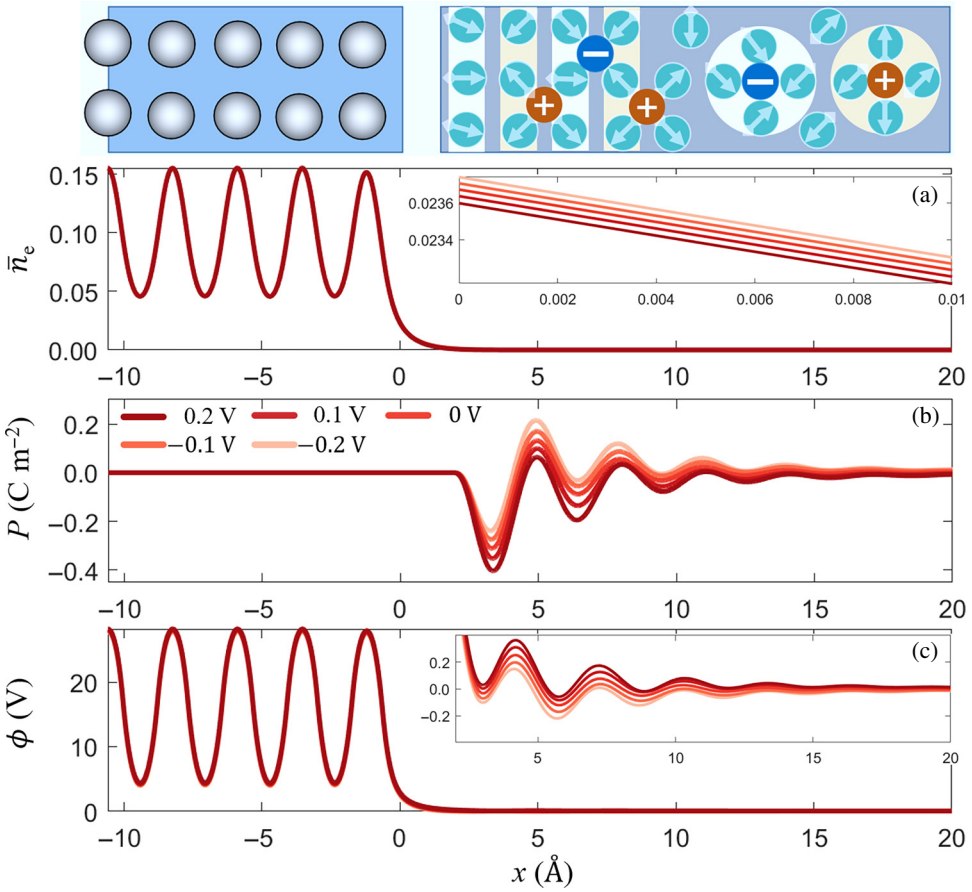

FIG. 2. Model results for the Ag(110)-0.1 M KPF_6 aqueous solution interface at five electrode potentials, referenced to the PZC, as indicated in the legends of (b): (a) distribution of the dimensionless electron density, with the inset presenting an enlarged view near the metal surface; (b) distribution of the solvent polarization; (c) distribution of the electric potential, with the inset showing an enlarged view on the solution side. In all these plots, the metal edge is located at $x = 0$. The top panel provides a schematic illustration of the electric double layer structure, featuring periodically arranged metal cationic cores, and layered structures of ions and solvent molecules near the metal surface.

electrons to spill out further into the solution. Figure 2(b) illustrates the spatial oscillations of solvent polarization. The amplitude of oscillations gradually decreases as the distance from the metal surface increases, eventually vanishing in the bulk solution. The oscillatory solvent polarization results in a corresponding oscillatory polarization charge. Therefore, a spatially damped oscillation in the electric potential is formed on the solution side, as shown in the inset of Fig. 2(c). The formation of the oscillatory solvent polarization stabilizes the interface via the term $K_\alpha(\nabla \cdot \mathbf{P})^2 = K_\alpha \rho_b^2$ in the grand potential, with a negative K_α. In the presence of a negative solvent polarization near the metal surface, oxygen atoms of water molecules are directed towards the metal surface, forming the oxygen-down configuration [89], whereas a positive solvent polarization means the hydrogen-down configuration. Valleys and peaks in Fig. 2(b) represent water molecules in opposite orientations, with alternating distribution. Water molecules closest to the metal surface exhibit a preference for the oxygen-down configuration, as observed in molecular dynamics simulations [42,90]. This is attributed to the electron spillover effect. The electrons spilt out from the metal surface induce a substantial potential drop that extends approximately 3 Å from the metal surface, as shown in the inset of Fig. 2(c). This potential drop tends to orient the oxygen atom of water molecules in the first layer towards the metal surface. Compared to the *ab initio* molecular dynamics results [42,90,91], the water layers are slightly farther away from the metal surface in our model. This is due to our simplified consideration of the repulsive interactions between water molecules and the metal surface. As the electrode potential gradually becomes more negative, the overall polarization field becomes more positive, as shown in Fig. 2(b). This implies that the hydrogen-down configuration is more favored at more negatively charged metal surfaces, as reported in computational [42,92] and experimental studies [89,93–95].

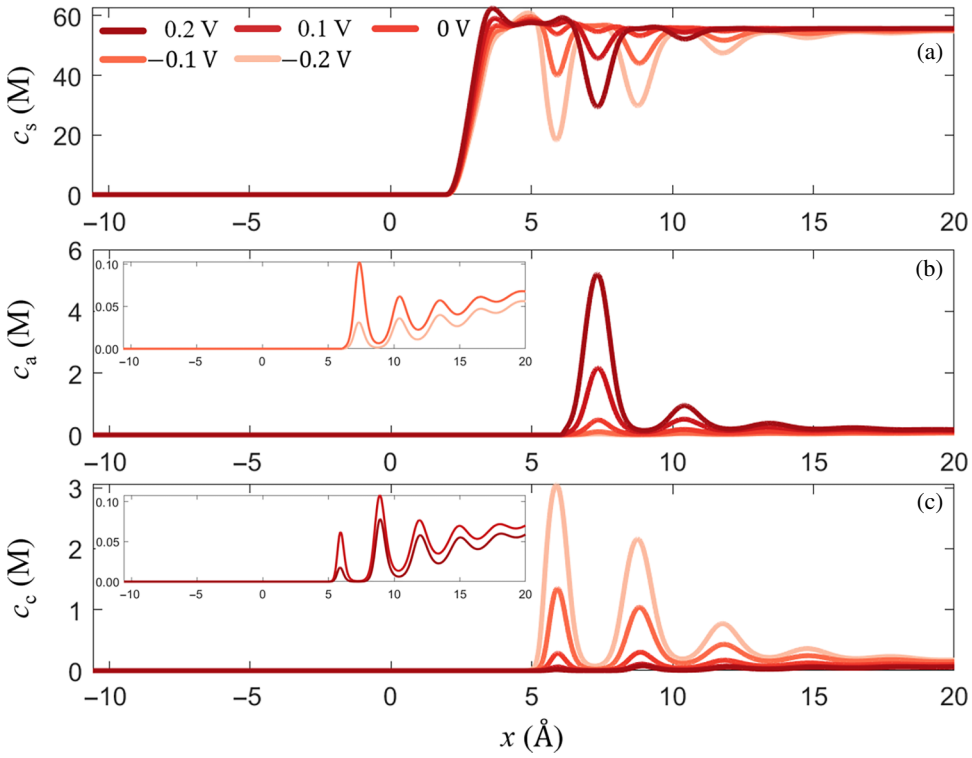

FIG. 3. Model results for the Ag(110)-0.1 M KPF_6 aqueous solution interface at five electrode potentials, referenced to the PZC, as indicated in the legend of (a): (a) distribution of the solvent concentration; (b) distribution of the anion concentration, with the inset presenting an enlarged view at negative potentials; (c) distribution of the cation concentration, with the inset presenting an enlarged view at positive potentials. In all of these plots, the metal edge is located at $x = 0$.

2. Layering

An oscillatory water polarization indicates water layering, which has recently been observed at the Ag(*hkl*)-NaOH aqueous solution interfaces using *in situ* surface x-ray diffraction measurements [51]. Figure 3(a) depicts the layered distributions of water molecules at the interface. As the electrode potential becomes more negative, the concentration of the oxygen-down water increases, while that of the hydrogen-down water decreases. These changes depict reorientation of water dipoles in response to the varying electric field at the interface. The alternating layers of water molecules with different net orientations generate local minima and maxima in electric potential, as shown in Fig. 2(c). The oscillatory electric field, along with short-range correlations with water molecules, leads to a layered pattern of ion distributions, as shown in Figs. 3(b) and 3(c). Both anions and cations are distributed in an alternating layered structure, with their peak concentrations rapidly decaying to bulk concentrations as they move away from the metal surface. Furthermore, due to weaker interactions with the metal surface, ions are unable to penetrate the water layer closest to the metal surface.

We observe that as the potential becomes more negative, the anion concentration in the first layer gradually decreases. However, as shown in the inset of Fig. 3(b), even at a potential as negative as −0.2 V vs PZC, the concentration of anions in the first layer remains approximately one-third of that in the bulk solution. In fact, at a potential of −0.1 V vs PZC, the anion concentration in the first layer even slightly exceeds the bulk concentration. The situation is opposite for cations, as shown in Fig. 3(c). This observation contrasts with classical double-layer theory, in which coions near the metal surface are expected to exhibit lower concentrations than those in the bulk solution. In our model, the anomalous accumulation of coions near the metal surface is attributed to the structured solvent stabilizing the coions. Another potential factor could be the specific adsorption of coions, which allows them adsorb on the metal surface irrespective of electrostatic repulsion. The adsorption of an ion near the metal surface is determined by a balance of the electrostatic and chemical interactions with the metal, as well as its compatibility within the solvent layers.

Recently, Yoo *et al*. have observed the apparent anion effect in the electrochemical CO_2 reduction reaction (eCO_2RR) [96]. Their experiments show that inorganic anions, i.e., perchlorate, sulfate, chloride, lead to higher overpotentials of eCO_2RR. This observation could be attributed to the non-negligible concentration of anions near the metal surface that remains even at negative surface

charge. This non-negligible concentration may result from the specific adsorption of anions and their interactions with the local solvent structure. Anions near the metal surface may destabilize the negatively charged transition and final state of the first elementary step in eCO_2RR [97], namely the formation of partially charged $CO_2^{\delta-}$ from CO_2 adsorption, which is generally accepted to be the rate-determining step of eCO_2RR [98,99].

Another notable feature revealed in Fig. 3 is that anions and cations approach the metal surface to different extents, each adjusting to better fit between solvent layers. This implies that a preset outer Helmholtz plane might be oversimplified [100]. Previous models, including ours [3,101–104], used the Frumkin corrections based on the notation of a reaction plane, often designated at the outer Helmholtz plane, to account for the local reaction conditions. While the reaction plane may be a reasonable approximation, a fixed reaction plane is oversimplified according to the foregoing analysis. Therefore, a detailed description of the structured solvent is certainly important for describing the local reaction conditions. The layered structure of ions delineated by our model can help identify the position of the reaction plane of electrochemical reactions, specifically referred to as the position of the peak concentration of ions in the first layer.

In summary, our theory captures the atomistic structure of the EDL, which is absent in classical EDL theories. The periodic arrangement of metal cation cores within the metal phase leads to periodically spatial oscillations in electron density and potential, as illustrated in the top schematic figure of Fig. 2. On the solution side, interfacial solvent molecules form a layered structure with alternating orientations due to short-range correlations, leading to a spatially damped oscillation in electric potential toward the solution bulk. Anions and cations also form layered structures, sandwiched between the solvent layers. Moving towards the solution bulk, the layered structures gradually vanish.

C. Parametric study

In this section, we use the calibrated model to study the influence of model parameters on the EDL structure and capacitance. The parametric study will be conducted in three groups. The first group contains parameters related to metal electronic properties, including the gradient coefficient in the electronic kinetic energy functional (θ_T) and the metal cationic charge density (n_{cc}^0). The second group focuses on the ion properties, including the radii of anions and cations (R_a and R_c), the strengths of their short-range correlations with solvent molecules (α_a and α_c), and the parameters describing the short-range interactions between ions and the metal surface (d_a^M, d_c^M, β_a, and β_c). The third group consists of parameters related to the solvent, including the static dielectric permittivity (ϵ_s), the high-frequency dielectric permittivity ($\epsilon_{\infty,S}$), the short-range correlation coefficients (K_α and K_β), and the parameters describing the short-range interactions between solvent molecules and the metal surface (d_s^M and β_s).

1. Metal electronic properties

Figures 4(a) and 4(b) show the C_{dl} curves as a function of $-\tilde{\mu}_e$, evaluated at three different values of θ_T and n_{cc}^0, respectively. All other parameters except the one under evaluation have their base values listed in Tables I–III. According to Eq. (68), $-\tilde{\mu}_e$ is proportional to ϕ_M. As θ_T increases to larger values, the C_{dl} curves shift rightward along the $-\tilde{\mu}_e$ axis. The value of $-\tilde{\mu}_e$ at the PZC, denoted

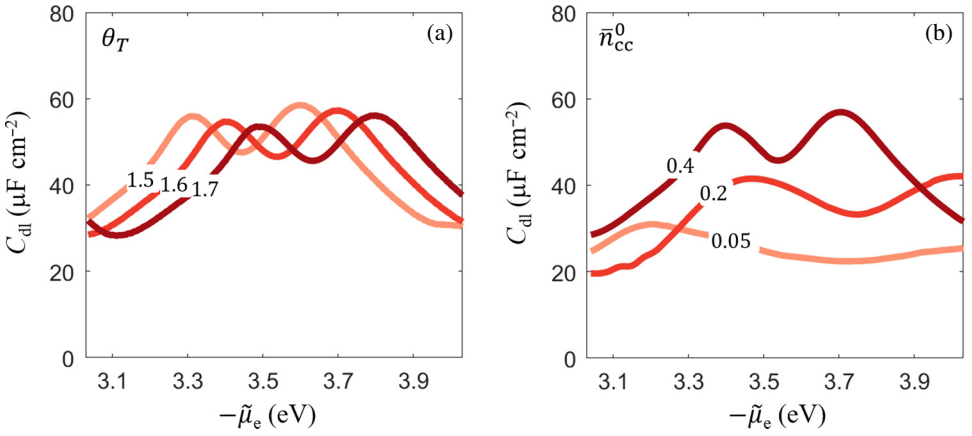

FIG. 4. Differential double-layer capacitance C_{dl} curves as a function of the negative of the electrochemical potential of electrons $-\tilde{\mu}_e$, which can be transformed into the electrode potential up to a constant. The parameters varied are (a) the gradient coefficient θ_T in the electronic kinetic energy functional, (b) the dimensionless charge density of metal cationic cores $\bar{n}_{cc}^0$, each evaluated at three levels. In this one-factor-at-a-time study, all other parameters except the one under evaluation have their base values listed in Tables I–III.

as $-\tilde{\mu}_{e,PZC}$, becomes more positive with increasing θ_T. Further, $-\tilde{\mu}_{e,PZC}$ is decomposed as follows:

$$-\tilde{\mu}_{e,PZC} = -\mu_e + e_0\phi_{M,PZC}, \tag{88}$$

where $\phi_{M,PZC}$ is the inner potential of the bulk metal at the PZC, which is mainly influenced by the surface dipoles, formed by electron spillover and solvent polarization [105, 106]. The chemical potential of metal electrons in the bulk is expressed as

$$\begin{aligned}\mu_e &= \frac{\partial t_{ni}}{\partial n_e} + \frac{\partial u_X}{\partial n_e} + \frac{\partial u_C}{\partial n_e} \\ &= e_{au}\left(\frac{\partial t_{TF}}{\partial \bar{n}_e} + (1+\theta_X s^2)\frac{\partial u_X^0}{\partial \bar{n}_e} + \frac{\partial u_C^0}{\partial \bar{n}_e} + u_X^0\theta_{XC}\frac{\partial s^2}{\partial \bar{n}_e}\right) \\ &\quad - \frac{3}{10}e_{au}(3\pi^2)^{\frac{2}{3}}s^2(\bar{n}_e)^{\frac{2}{3}}\theta_T. \end{aligned} \tag{89}$$

As shown in Eq. (89), μ_e is independent of θ_T due to the uniform electron density in the jellium model. However, at larger θ_T, electrons at the metal surface possess higher kinetic energy, allowing them to spillout farther from the metal surface. Enhanced spillover leads to a larger surface dipole potential at the metal surface, shifting the PZC positively, as shown in Fig. 4(a).

Different metals have different values of n_{cc}^0, which exerts a significant impact on C_{dl}, especially the Helmholtz layer capacitance [37]. As shown in Fig. 4(b), the C_{dl} curve is elevated at larger n_{cc}^0 because more electrons are presented to screen the electric field in the EDL. A nonmonotonic dependence of $-\tilde{\mu}_{e,PZC}$ on n_{cc}^0 is observed. In the examined range, $-\mu_e$ decreases with increasing n_{cc}^0 in Eq. (88) [58]. However, $\phi_{M,PZC}$ increases since more electrons spillover from the metal surface, resulting in larger surface dipole potential and, consequently, larger $\phi_{M,PZC}$. This is supported by the calculated dipole potential using a jellium-hard-sphere-electrolyte model [37], which exhibits a monotonically increasing trend of dipole potential with n_{cc}^0, aligning closely with the experimentally estimated dipole potential for different metals [107]. The opposing trends in $-\mu_e$ and $\phi_{M,PZC}$ with respect to n_{cc}^0 lead to the nonmonotonic variation of the PZC.

The same metal but with different crystal faces should have the same values of n_{cc}^0, but different values of θ_T are expected. Figure 5 compares the experimentally measured C_{dl} profiles of Ag(110) and Ag(100) in a 0.1 M KPF_6 aqueous solution, exhibiting a positive shift of 0.11 V in the PZC from the Ag(110) to Ag(100) interface. By solely tuning the values of θ_T from 1.585 at the Ag(110) interface to 1.703 at the Ag(100) interface, while keeping all other parameters at their base values, the simulated results agree well with the experimental C_{dl} curve at the Ag(100) interface. This implies that electrons at the Ag(100) surface possess higher kinetic energy and exhibit greater spillover.

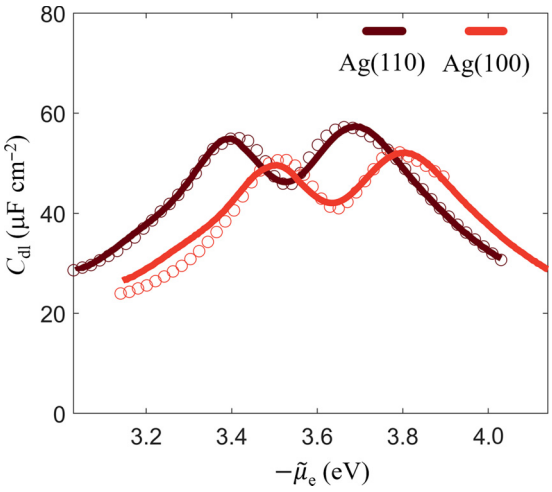

FIG. 5. Model (lines) and experimental results (circles) of the differential double-layer capacitance C_{dl} at Ag(110) and Ag(100) in 0.1 M KPF_6 aqueous solution as a function of the negative of the electrochemical potential of electrons $-\tilde{\mu}_e$, which can be transformed into the electrode potential up to a constant. The experimental data at Ag(110) and Ag(100), measured by Valette, are corrected using a suggested roughness factor of 1.15 [28] and 1.07 [27], respectively. In the modeling of the Ag(100)-0.1 M KPF_6 aqueous solution interface, only θ_T is tuned to 1.703 while all other parameters have their base values.

This electron spillover effect contributes to the observed positive shift in the PZC.

2. Ion properties

Figures 6(a) and 6(b) show the influence of anion and cation sizes on the C_{dl} curves, respectively. The anionic peak of the C_{dl} curve, corresponding to anion crowding, is smaller and appears at less positive potential for larger anions. Similar behaviors are observed for the cationic peak corresponding to cation crowding. The size behaviors are similar to those of classical EDL theories [108]. If the ion radius is gradually reduced to a certain threshold, as shown in the inset of Fig. 6(a), the C_{dl} curve becomes independent of the ion radius. In this scenario, the corresponding ionic peak and the subsequent decrease in capacitance are attributed to the dielectric screening effect of the solvent, which reduces the dielectric permittivity near the metal surface. In other words, the ionic peak observed in the C_{dl} curve arises from the competition between the ion crowding effect and the dielectric screening effect. Once the ion size falls below a critical value, the dielectric screening effect becomes dominant.

As shown in Fig. 9, Valette's experiments reveal that the electrode potential at the anionic peak remains nearly the same at both the Ag(110)-KPF_6 and Ag(110)-$NaClO_4$ aqueous solution interfaces. Nevertheless, the anionic peak is more pronounced at the Ag(110)-$NaClO_4$ aqueous solution interface. Additionally, the capacitance at the PZC is

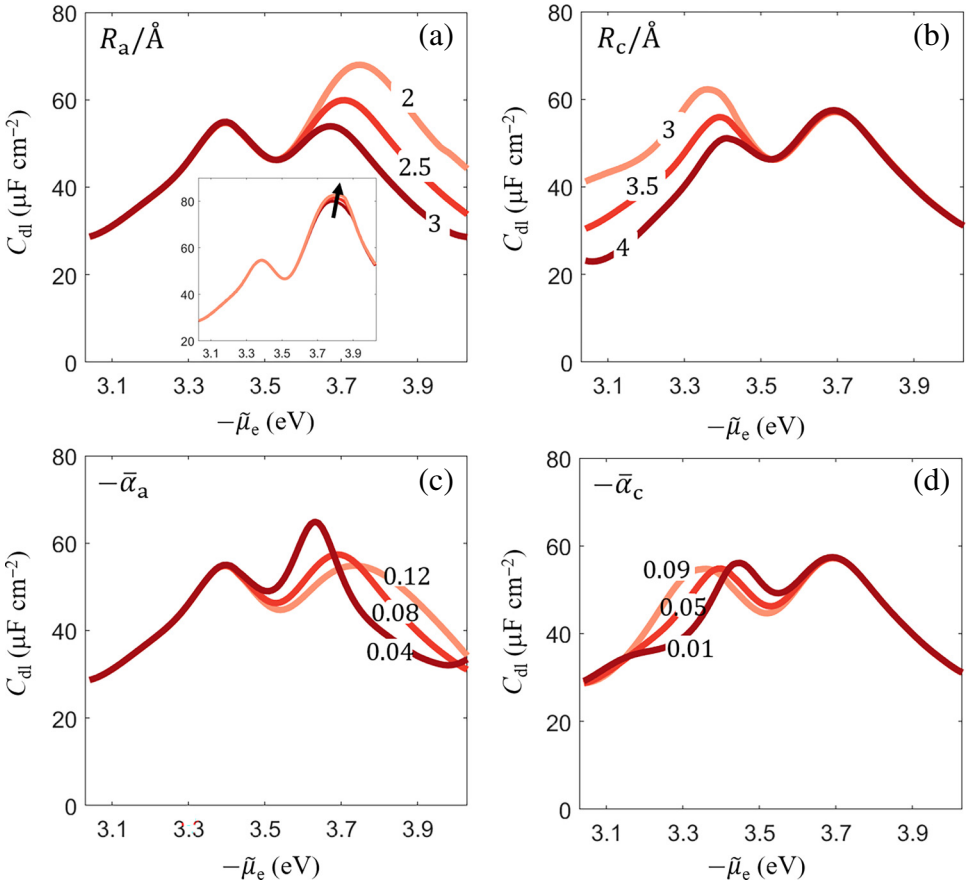

FIG. 6. Differential double layer-capacitance C_{dl} curves as a function of the negative of the electrochemical potential of electrons $-\tilde{\mu}_e$, which can be transformed into the electrode potential up to a constant. The parameters varied are (a) the anion radius R_a, (b) the cation radius R_c, (c) the dimensionless strength of short-range correlation between the anion and solvent molecules $\bar{\alpha}_a$, and (d) the dimensionless strength of short-range correlation between the cation and solvent molecules $\bar{\alpha}_c$, each evaluated at three levels. The inset in (a) displays the C_{dl} curves for decreasing anion radii of 1.3, 1.2, and 1.1 Å along the direction indicated by the arrow. In this one-factor-at-a-time study, all other parameters except the one under evaluation have their base values listed in Tables I–III.

higher at the Ag(110)-$NaClO_4$ aqueous solution interface compared to the Ag(110)-KPF_6 aqueous solution interface. These observations indicate that the ionic size alone is insufficient to fully explain the effects of ion properties on the C_{dl} curve. As a refinement beyond the classical EDL theory, our model considers not only the ion size but also their short-range correlations with solvent molecules and their short-range interactions with the metal.

Figures 6(c) and 6(d) show that as α_a and α_c become less negative, the anionic and cationic peaks of the C_{dl} curves narrow, respectively. To rationalize these observations, we focus on the effect of α_a on the C_{dl} curve as an example. The distributions of the electric potential at the PZC for various values of α_a are shown in Fig. 7(a). It is evident that α_a has a minor effect on the oscillations in the electric potential, which implies a correspondingly limited impact on the interfacial solvent structure. However, as discussed in Eq. (17), when α_a becomes less negative, the short-range correlations between anions and solvent molecules are less effective at screening the electrostatic forces exerted by the solvent polarization charges on anions. This diminished screening amplifies the influence of the local electric potential peak on the anions. Consequently, more anions are located in the space between solvent layers, enhancing anion layering at a less negative α_a, as illustrated in Fig. 7(b).

Therefore, an enhanced anion layering at less negative α_a reduces the effective thickness of the EDL and results in an enhanced ion crowding effect. The reduction in EDL thickness increases C_{dl} in the potential region just above the PZC, while the enhanced ion crowding effect shifts the anionic peak to a less positive potential. Additionally, anions are drawn closer to the metal surface, particularly within the first anion layer, where the dielectric screening effect becomes more pronounced. This pronounced screening reduces the effective dielectric permittivity at less negative α_a, which in turn causes a steeper decline in the C_{dl} curve at more positive potentials. Collectively, the enhanced anion layering accounts for the narrower anionic peak observed in the C_{dl} profile at less negative α_a. The

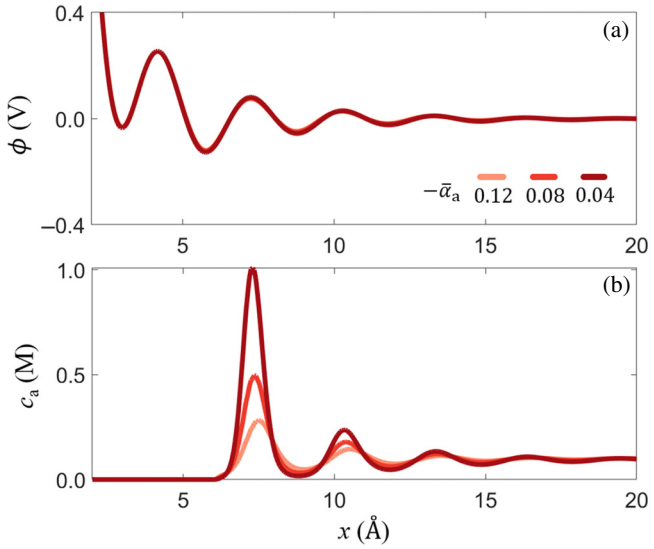

FIG. 7. The distributions of (a) the electric potential and (b) the anion concentration at the PZC of the differential double-layer capacitance C_{dl} profiles in Fig. 6(c), for different dimensionless strengths of short-range correlations between the anion and solvent molecules $\bar{\alpha}_a$, as indicated in (a). The metal edge is located at $x = 0$.

impact of α_c on the cationic peak of the C_{dl} profile is the same.

Different ions exhibit varying strengths of short-range interactions with the metal. Figure 8 shows the impact of these interaction parameters on the C_{dl} profiles, including the previously defined effective equilibrium distances and coefficients in the Morse potentials. A smaller d_a^M indicates a weaker repulsive force between anions and the metal surface, allowing anions to approach closer to the metal surface at potentials positive to the PZC. As discussed, this reduces the effective thickness and dielectric permittivity of the EDL, leading to a narrower anionic peak in the C_{dl} curve at smaller d_a^M, as shown in Fig. 8(a). The impact of d_c^M on the cationic peak of the C_{dl} profile, as shown in Fig. 8(b), follows a similar pattern. As for the coefficients in the Morse potentials of ions (β_a and β_c), they have negligible impact on the C_{dl} profiles, as shown in Figs. 8(c) and 8(d).

The ion parameters R_i, α_i, and d_i^M significantly impact the position and shape of the ionic peaks in the C_{dl} curves. Additionally, a smaller d_i^M or a less negative α_i can yield a larger capacitance at the PZC. This is because reducing d_i^M and decreasing the negativity of α_i, respectively, increase

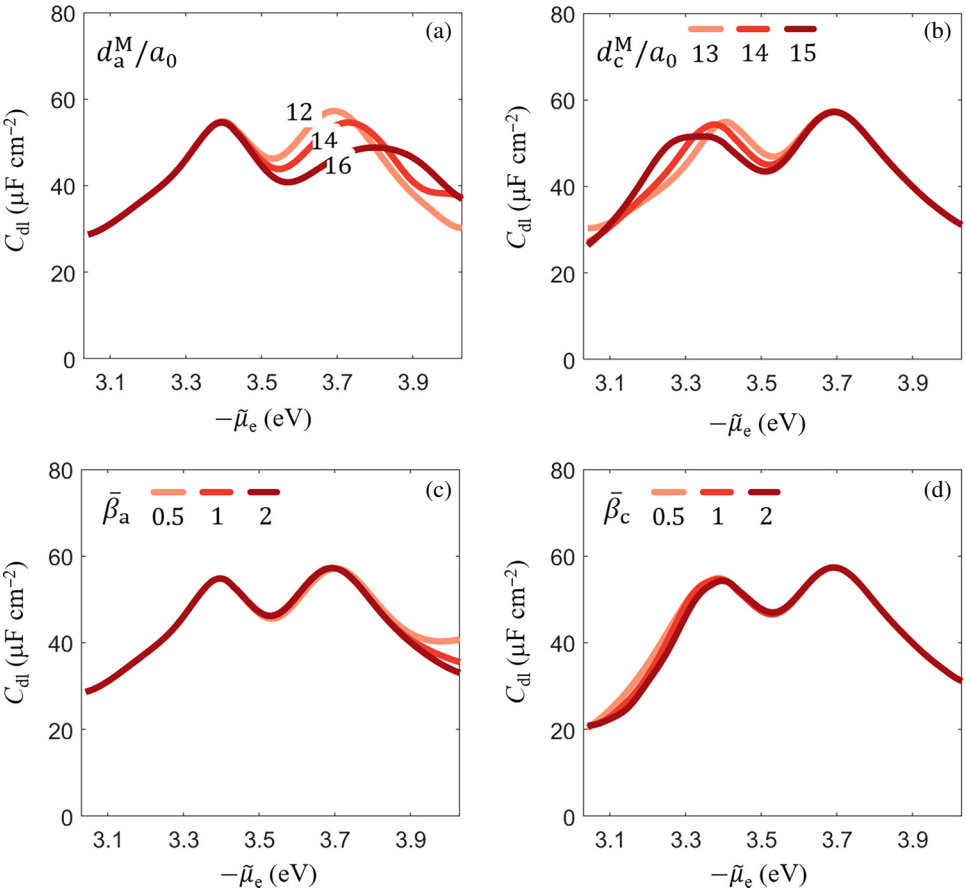

FIG. 8. Differential double-layer capacitance C_{dl} curves as a function of the negative of the electrochemical potential of electrons $-\tilde{\mu}_e$, which can be transformed into the electrode potential up to a constant. The parameters varied are (a) the effective equilibrium distance of anions d_a^M, (b) the effective equilibrium distance of cations d_c^M, (c) the dimensionless coefficient in the Morse potential for anions β_a, (d) the dimensionless coefficient in the Morse potential for cations β_c, each evaluated at three levels. In this one-factor-at-a-time study, all other parameters except the one under evaluation have their base values listed in Tables I–III.

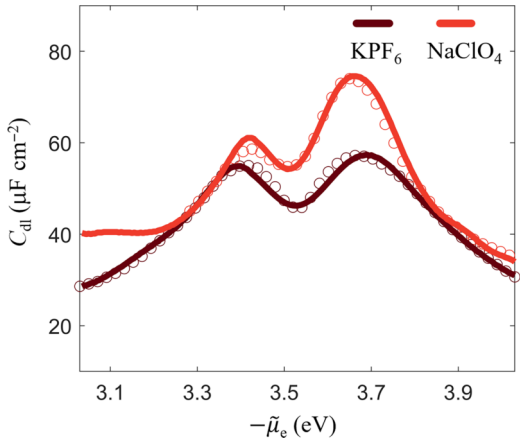

FIG. 9. Model (lines) and experimental results (circles) of the differential double-layer capacitance C_{dl} at Ag(110) in 0.1 M KPF_6 and 0.1 M $NaClO_4$ aqueous solutions as a function of the negative of the electrochemical potential of electrons $-\tilde{\mu}_e$, which can be transformed into the electrode potential up to a constant. The experimental data at Ag(110), measured by Valette, are corrected using a suggested roughness factor of 1.15 [28]. In the simulation of Ag(110)-0.1 M $NaClO_4$ aqueous solution interface, only the ion properties, as shown in Table IV, are tuned, while all other parameters remain at their base values, as listed in Tables I–III.

the thickness of the diffuse layer and the capacity of the solvent layers to accommodate ions, both of which inherently enhance the EDL's ability to store ionic charges. Naturally, these two parameters are not only related to the type of ions but also to the types of metals and solvents. Through the combined influence of these ion properties, the C_{dl} curve at the Ag(110)-$NaClO_4$ aqueous solution interface can be reproduced, as shown in Fig. 9. We emphasize that only the ion parameters are altered, while all other parameters are maintained at their base values in Tables I–III. The ion parameters for KPF_6 and $NaClO_4$ electrolytes are listed in Table IV. The tightly solvated Na^+ cations are smaller than the tightly solvated K^+ cations [78], while the sizes of PF_6^- and ClO_4^- anions are comparable. Compared to the KPF_6 electrolyte solution, the $NaClO_4$ electrolyte solution possesses less negative α_i for Na^+ and ClO_4^-, resulting in increased capacitance at both the ionic peaks and PZC. Additionally, ClO_4^- can approach the Ag(110) surface more closely than PF_6^-, consistent with Valette's findings that ClO_4^- exhibits a stronger specific adsorption strength compared to PF_6^- [28].

3. Solvent properties

The solvent significantly influences the Helmholtz layer [20,109] and the diffuse layer [110] of the EDL structure. In the present context, these solvent properties include basic static dielectric properties, short-range correlations between solvent molecules, and short-range interactions between the solvent and the metal surface. The solvent dependence of C_{dl} is determined by all solvent properties, rendering it difficult to decouple the influence of a single property without the aid of a model [86,111].

TABLE IV. Parameters of ion properties at Ag(110) in 0.1 M KPF_6 and 0.1 M $NaClO_4$ aqueous solutions, including the ion radius R_i, the dimensionless strength of short-range correlations between ions and solvent molecules $\bar{\alpha}_i$, the effective equilibrium distance of ions from the metal surface d_i^M, and the dimensionless coefficient in the Morse potential for ions $\bar{\beta}_i$.

Ion parameters	R_i/Å	$\bar{\alpha}_i$	d_i^M/a_0	$\bar{\beta}_i$
Tightly solvated K^+	3.6	−0.05	13.3	0.19
Tightly solvated Na^+	3.25	−0.022	13.3	0.15
Bare PF_6^-	2.7	−0.081	11.6	4.5
Bare ClO_4^-	2.75	−0.04	9.4	1

In the theoretical model, static dielectric properties of the solvent, which dictate its ability to screen the interfacial electric field, are delineated by two key parameters: the high-frequency dielectric permittivity ($\epsilon_{\infty,S}$) and the effective dipole moment (p_{eff}) of the solvent. Their influences on C_{dl} curves are displayed in Figs. 10(a) and 10(b). As expected, an elevated C_{dl} profile is obtained at larger $\epsilon_{\infty,S}$ and p_{eff}. When p_{eff} increases, the solvent can better screen the electric field generated by electron spillover near the metal surface. This leads to a decrease in $\phi_{M,PZC}$ and, as a result, a negative shift in the PZC. Similarly, increasing $\epsilon_{\infty,S}$ also improves the solvent's screening capability, but its primary impact on the PZC arises from the enhancement of local screening within the region approximately 2 Å above the metal edge, as shown in Eq. (82). In a recent work, we have discussed the influence of static dielectric properties on the PZC at the Au(111)-KPF_6 interface [86]. The static dielectric properties primarily influence the overall magnitude of the PZC of C_{dl} curves but have little impact on their shapes.

In addition to the static dielectric properties, the theory incorporates short-range correlations between solvent molecules, controlled by K_α and K_β in the short-range correlation functional. Their influence on the C_{dl} profile is shown in Figs. 11(a) and 11(b). When K_α becomes more negative or when K_β decreases, the C_{dl} at the PZC is elevated, the anionic and cationic peaks are closer, and the PZC shifts to more negative potentials. It is observed that a more negative value of K_α leads to a more oscillatory solvent polarization, as shown in Fig. 12(a). As K_α approaches zero, the oscillations gradually diminish. A more oscillatory solvent polarization implies that solvent molecules near the metal surface more effectively screen the electric field generated from metal electron spillover, thereby lowering $\phi_{M,PZC}$ and shifting the PZC to a more negative value. The increased oscillation in solvent polarization at more negative K_α causes a more oscillatory

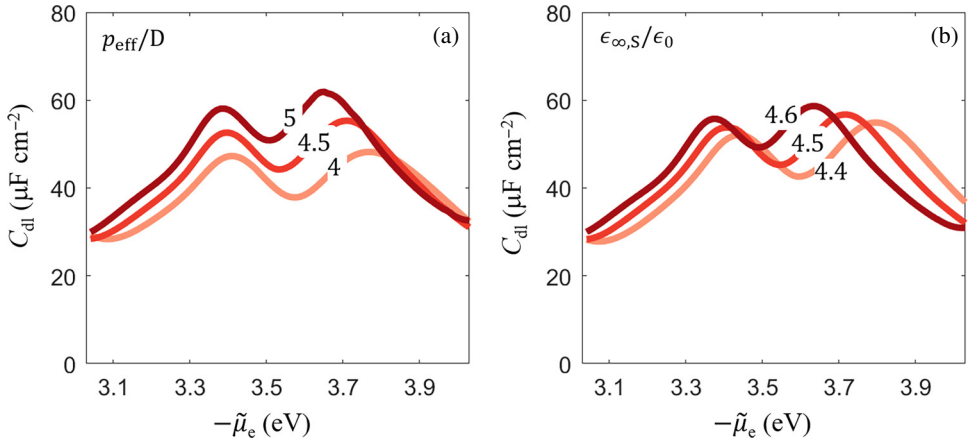

FIG. 10. Differential double-layer capacitance C_{dl} curves as a function of the negative of the electrochemical potential of electrons $-\tilde{\mu}_{\mathrm{e}}$, which can be transformed into the electrode potential up to a constant. The parameters varied are (a) the effective dipole moment p_{eff}, (b) the high-frequency dielectric permittivity $\epsilon_{\infty,\mathrm{S}}$, each evaluated at three levels. In this one-factor-at-a-time study, other parameters except the one under evaluation have their base values listed in Tables 1–III.

distribution of the electric potential on the solution side, facilitating a more layered structure of ions, as shown in Fig. 12(b). The more layered structure allows more ions to be present within the solvent layers, causing an increase in C_{dl} at the PZC. As discussed, a more layered structure of ions narrows the ionic peak in the C_{dl} curve. Additionally, at a more negative K_α, Fig. 12(a) shows that solvent molecules exhibit a more ordered orientation within each layer. This implies a lower dielectric permittivity at the interface, which in turn leads to a steeper decrease in C_{dl} at potentials far from the PZC. The mechanism of how K_β affects the C_{dl} curve is similar, as Fig. S1 in the Supplemental Material [76] shows a more oscillatory solvent polarization and a more layered interface at smaller K_β, akin to the situation observed with a more negative K_α. The consideration of short-range correlations among solvent molecules, which lead to a layered structure at the interface, contributes to the increase in capacitance at the PZC and the narrowing of ionic peaks. This is the primary reason why the model results of DPPFT better align with experimental observations.

DPPFT inherently accounts for the effects of short-range interactions between solvent molecules and the metal surface on the EDL structure and properties. This consideration is not explicitly considered in the theory proposed by Hedley *et al.* [46], or that by Blossey and Podgornik [47,48]. Figure 13 highlights the significant impact of the short-range interaction parameters $d_{\mathrm{s}}^{\mathrm{M}}$ and β_{s} on the C_{dl} profile. At a smaller $d_{\mathrm{s}}^{\mathrm{M}}$, we observe a more negative PZC, a higher C_{dl} at the PZC, and a reduced distance between

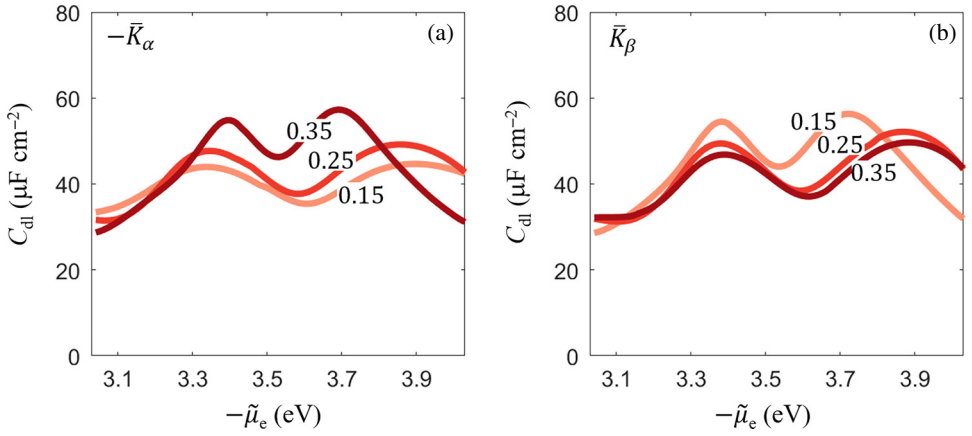

FIG. 11. Differential double-layer capacitance C_{dl} curves as a function of the negative of the electrochemical potential of electrons $-\tilde{\mu}_{\mathrm{e}}$, which can be transformed into the electrode potential up to a constant. The parameters varied are the dimensionless coefficients in the short-range correlation functional of solvent molecules, (a) $\bar{K}_\alpha$ and (b) $\bar{K}_\beta$, each evaluated at three levels. In this one-factor-at-a-time study, all other parameters except the one under evaluation have their base values listed in Tables I–III.

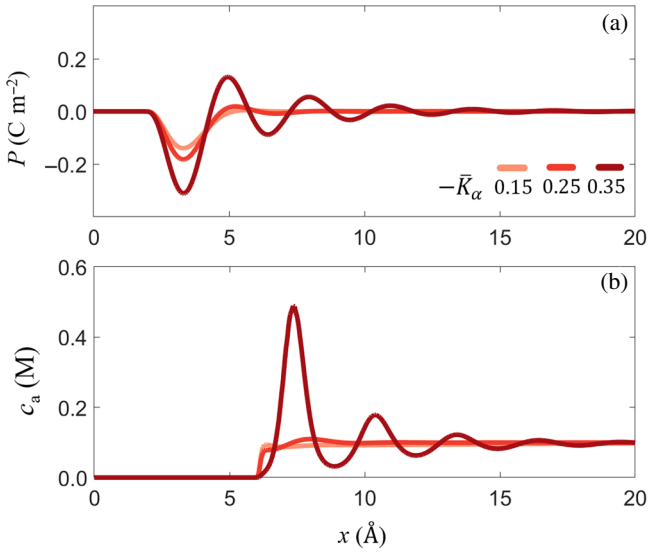

FIG. 12. Distributions of (a) the solvent polarization and (b) the anion concentration at the PZC of the differential double-layer capacitance C_{dl} profiles shown in Fig. 11(a), for different values of dimensionless coefficient $\bar{K}_\alpha$, in the short-range correlation functional of solvent molecules, as indicated in (a). The metal edge is located at $x = 0$.

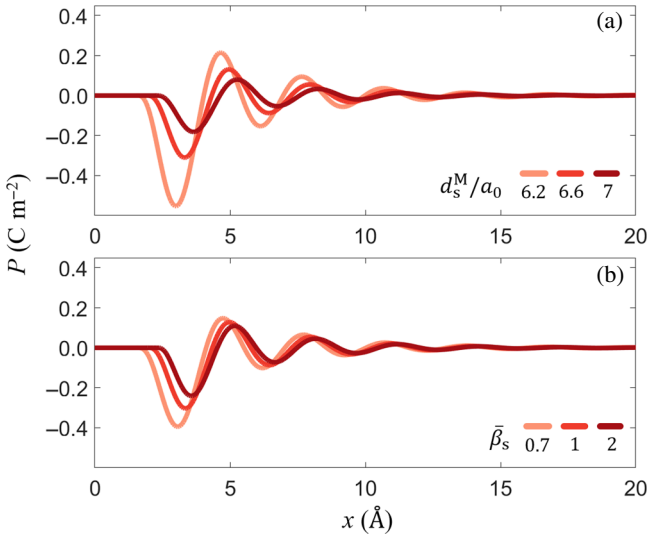

FIG. 14. Distributions of the solvent polarization at the PZC of the differential double-layer capacitance C_{dl} profiles shown in Fig. 13, for different values of (a) the effective equilibrium distance of solvent molecules d_s^M, and (b) the dimensionless coefficient β_s in the Morse potential for solvent molecules, as indicated. The metal edge is located at $x = 0$.

anionic peak and cationic peak of the C_{dl} curve. A similar trend is evident for smaller values of β_s , as shown in Fig. 13(b).

Figure 14 shows the distributions of the solvent polarization for various values of d_s^M and β_s. The EDL becomes more oscillatory and, therefore, more layered at smaller values of d_s^M or β_s. A more layered interface, as previously discussed, accounts for the observed trends in the C_{dl} profile with decreasing d_s^M and β_s in Fig. 13. We also notice that the oscillatory distribution of the solvent polarization shifts closer to the metal surface at smaller d_s^M and β_s. This promotes ion layering nearer to the metal surface, thereby facilitating the electron transfer between ions and the metal surface. The effects of d_s^M and β_s on the EDL structure can be attributed to the impact of metal electron spillover on solvent molecules. Smaller values of d_s^M and β_s allow solvent molecules to approach the metal surface more closely, exposing them to a stronger electric field generated by the electron spillover. The dielectric response of solvent molecules to this intensified field induces a

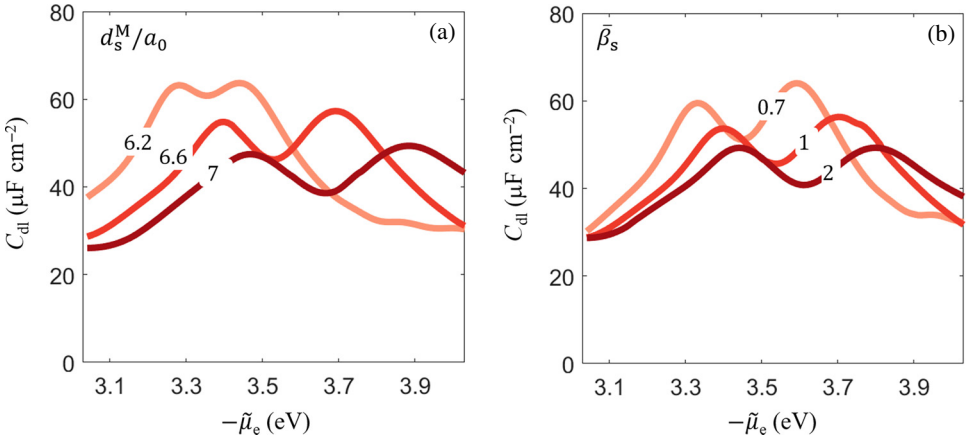

FIG. 13. Differential double-layer capacitance C_{dl} curves as a function of the negative of the electrochemical potential of electrons $-\tilde{\mu}_e$, which can be transformed into the electrode potential up to a constant. The parameters varied are (a) the effective equilibrium distance of solvent molecules d_s^M, (b) the dimensionless coefficient β_s in the Morse potential for solvent molecules, each evaluated at three levels. In this one-factor-at-a-time study, all other parameters except the one under evaluation have their base values listed in Tables I–III.

more pronounced oxygen-down orientation in the first solvent layer. Then the electrostatic interactions between solvent layers promote more ordered orientations of solvent molecules in the subsequent layers. The more ordered orientation of solvent molecules in each layer contributes to a more oscillatory distribution of solvent polarization.

IV. CONCLUSIONS

We have developed a computationally efficient density-potential-polarization functional theory for the modeling of EDLs under constant-potential conditions. The DPPFT approach effectively captures two essential features of an EDL at a continuum level, namely the electronic response and structured solvent. Calibrated with existing capacitance data of the Ag(110)-KPF_6 aqueous solution interface [28], the model unveils atomistic details of the EDL structure associated with profiles of double-layer capacitance, including electron spillover, spatially damped oscillations in solvent polarization and electric potential extending toward the bulk solution, and the layered structure of ions. Solvent molecules form a layered structure with alternating orientations near the metal surface, with anion and cation layers dispersed between the solvent layers. The compatibility of coions with the local solvent structure allows us to explain why there is an excess of them in the EDL, a phenomenon absent in classical EDL theories. The ion layering provides a physically reasonable basis for identifying the reaction plane as the position of peak ion concentration in the first layer.

We conducted a parametric study with the calibrated model to explore the influence of electronic, ion, and solvent properties on the EDL structure and capacitance. Thanks to an explicit account of the metal electron spillover effect and combined effects of ion properties, the model well reproduces and explains the experimental capacitances observed across different crystal faces and in various electrolyte solutions. The gradient coefficient in the electronic kinetic energy functional affects the PZC monotonically via altering the surface potential, while the charge density of metal cationic cores exhibits a nonmonotonic relationship with the PZC by simultaneously tuning the surface potential and the electron chemical potential in the bulk metal. The model describes the static dielectric properties of the solvent in terms of two key parameters: its high-frequency dielectric permittivity and effective dipole moment. The solvent with larger values of those parameters more effectively screens the interfacial electric field, resulting in an increased capacitance and a negative shift in PZC.

We revealed that intensified ion layering elevates the capacitance at the PZC and narrows the ionic peaks in the double-layer capacitance profile. Ion layering is strongly influenced by short-range correlations and/or interactions between ions and solvent molecules, between solvent molecules, and between solvent molecules and the metal surface. Weaker short-range correlations between ions and solvent molecules result in less effective screening of the electrostatic field between solvent layers, allowing more ions to be accommodated within these layers. Interfacial oscillations are enhanced in the presence of stronger short-range correlations between solvent molecules, and stronger short-range interactions between solvent molecules and the metal surface. The latter is attributed to enhanced electron spillover effects on interfacial solvent molecules. A more oscillatory interface shifts the PZC negatively and promotes a more layered ion structure.

ACKNOWLEDGMENTS

M.Z. is financially supported by the China Scholarship Council to study abroad in Jülich. M.Z. and Y.C. thank the financial support from the National Natural Science Foundation of China under Grant No. 22172151. J.H. is supported by the Initiative and Networking Fund of the Helmholtz Association (Grant No. VH-NG-1709). M.Z. acknowledges financial support from Forschungszentrum Jülich GmbH, received within the framework of the Helmholtz program Materials and Technologies for Energy Transportation under the topic Chemical Energy Carriers and the subtopic Electrochemistry for hydrogen.

[1] J. Wu, Understanding the electric double-layer structure, capacitance, and charging dynamics, Chem. Rev. **122**, 10821 (2022).
[2] L. D. Chen, M. Urushihara, K. Chan, and J. K. Nørskov, Electric field effects in electrochemical CO_2 reduction, ACS Catal. **6**, 7133 (2016).
[3] X. Zhu, J. Huang, and M. Eikerling, pH effects in a model electrocatalytic reaction disentangled, JACS Au **3**, 1052 (2023).
[4] S. Kondrat, G. Feng, F. Bresme, M. Urbakh, and A. A. Kornyshev, Theory and simulations of ionic liquids in nanoconfinement, Chem. Rev. **123**, 6668 (2023).
[5] P. M. Biesheuvel and M. Z. Bazant, Analysis of ionic conductance of carbon nanotubes, Phys. Rev. E **94**, 050601 (2016).
[6] A. Levy, J. P. de Souza, and M. Z. Bazant, Breakdown of electroneutrality in nanopores, J. Colloid Interface Sci. **579**, 162 (2020).
[7] E. Secchi, A. Niguès, L. Jubin, A. Siria, and L. Bocquet, Scaling behavior for ionic transport and its fluctuations in individual carbon nanotubes, Phys. Rev. Lett. **116**, 154501 (2016).
[8] R. T. Mathias, G. J. Baldo, K. Manivannan, and S. Mclaughlin, in *Electrified Interfaces in Physics, Chemistry and Biology*, edited by R. Guidelli (Springer Netherlands, Dordrecht, 1992), pp. 473–490.
[9] B. Roux, T. Allen, S. Bernèche, and W. Im, Theoretical and computational models of biological ion channels, Q. Rev. Biophys. **37**, 15 (2004).

[10] K. Kristiansen, M. Valtiner, G. W. Greene, J. R. Boles, and J. N. Israelachvili, Pressure solution – The importance of the electrochemical surface potentials, Geochim. Cosmochim. Acta **75**, 6882 (2011).

[11] W. Schmickler and E. Santos, *Interfacial Electrochemistry* (Springer Science & Business Media, New York, 2010).

[12] A. J. Bard, L. R. Faulkner, and H. S. White, *Electrochemical Methods: Fundamentals and Applications* (John Wiley & Sons, New York, 2022).

[13] C. W. Outhwaite, Towards a mean electrostatic potential treatment of an ion-dipole mixture or a dipolar system next to a plane wall, Mol. Phys. **48**, 599 (1983).

[14] C. W. Outhwaite and L. B. Bhuiyan, A modified Poisson–Boltzmann equation in electric double layer theory for a primitive model electrolyte with size-asymmetric ions, J. Chem. Phys. **84**, 3461 (1986).

[15] J. J. Bikerman, XXXIX. Structure and capacity of electrical double layer, London, Edinburgh Dublin Philos. Mag. J. Sci. **33**, 384 (1942).

[16] E. Gongadze and A. Iglič, Asymmetric size of ions and orientational ordering of water dipoles in electric double layer model - An analytical mean-field approach, Electrochim. Acta **178**, 541 (2015).

[17] E. Gongadze, A. Velikonja, Š Perutkova, P. Kramar, A. Maček-Lebar, V. Kralj-Iglič, and A. Iglič, Ions and water molecules in an electrolyte solution in contact with charged and dipolar surfaces, Electrochim. Acta **126**, 42 (2014).

[18] A. Iglič, E. Gongadze, and V. Kralj-Iglič, Differential capacitance of electric double layer – Influence of asymmetric size of ions, thickness of stern layer and orientational ordering of water dipoles, Acta Chim. Slov. **66**, 534 (2019).

[19] J. Huang, A. Malek, J. Zhang, and M. H. Eikerling, Non-monotonic surface charging behavior of platinum: A paradigm change, J. Phys. Chem. C **120**, 13587 (2016).

[20] J. Huang, Zooming into the inner Helmholtz plane of Pt(111)–aqueous solution interfaces: Chemisorbed water and partially charged ions, JACS Au **3**, 550 (2023).

[21] M. Z. Bazant, B. D. Storey, and A. A. Kornyshev, Double layer in ionic liquids: Overscreening versus crowding, Phys. Rev. Lett. **106**, 4 (2011).

[22] Z. A. H. Goodwin, G. Feng, and A. A. Kornyshev, Mean-field theory of electrical double layer in ionic liquids with account of short-range correlations, Electrochim. Acta **225**, 190 (2017).

[23] D. C. Grahame and R. Parsons, Components of charge and potential in the inner region of the electrical double layer: Aqueous potassium chloride solutions in contact with mercury at 25°, J. Am. Chem. Soc. **83**, 1291 (1961).

[24] D. C. Grahame, The electrical double layer and the theory of electrocapillarity, Chem. Rev. **41**, 441 (1947).

[25] R. Parsons and N. F. Mott, The structure of the mercury-electrolyte interphase in the presence of thiourea, Proc. R. Soc. London, Ser. A 261, 79 (1997).

[26] G. Valette, Double layer on silver single crystal electrodes in contact with electrolytes having anions which are slightly specifically adsorbed: Part III. The (111) face, J. Electroanal. Chem. Interfacial Electrochem. **269**, 191 (1989).

[27] G. Valette, Double layer on silver single crystal electrodes in contact with electrolytes having anions which are slightly specifically adsorbed: Part II. The (100) face, J. Electroanal. Chem. Interfacial Electrochem. **138**, 37 (1982).

[28] G. Valette, Double layer on silver single-crystal electrodes in contact with electrolytes having anions which present a slight specific adsorption: Part I. The (110) face, J. Electroanal. Chem. Interfacial Electrochem. **122**, 285 (1981).

[29] A. Hamelin, T. Vitanov, E. Sevastyanov, and A. Popov, The electrochemical double layer on sp metal single crystals, J. Electroanal. Chem. Interfacial Electrochem. **145**, 225 (1983).

[30] S. Trasatti and L. M. Doubova, Crystal-face specificity of electrical double-layer parameters at metal/solution interfaces, J. Chem. Soc. Faraday Trans. **91**, 3311 (1995).

[31] S. Trasatti, Structure of the metal/electrolyte solution interface: New data for theory, Electrochim. Acta **36**, 1659 (1991).

[32] Kasinath Ojha, Katharina Doblhoff-Dier, and Marc TM Koper, Double-layer structure of the Pt(111)–aqueous electrolyte interface, Proc. Natl. Acad. Sci. **119**, e211601 6119 (2022).

[33] L. Zhang and J. Huang, Measurement and interpretation of the double layer capacitance of Pt(111)/aqueous solution interfaces, Curr. Opin. Electrochem. **42**, 101419 (2023).

[34] K. Doblhoff-Dier and M. T. M. Koper, Electric double layer of Pt(111): Known unknowns and unknown knowns, Curr. Opin. Electrochem. **39**, 101258 (2023).

[35] A. A. Kornyshev, Metal electrons in the double layer theory, Electrochim. Acta **34**, 1829 (1989).

[36] W. Schmickler, Electronic effects in the electric double layer, Chem. Rev. **96**, 3177 (1996).

[37] W. Schmickler and D. Henderson, The interphase between jellium and a hard sphere electrolyte. A model for the electric double layer, J. Chem. Phys. **80**, 3381 (1984).

[38] J. P. Badiali, M. L. Rosinberg, F. Vericat, and L. Blum, A microscopic model for the liquid metal-ionic solution interface, J. Electroanal. Chem. Interfacial Electrochem. **158**, 253 (1983).

[39] W. Schmickler, A jellium-dipole model for the double layer, J. Electroanal. Chem. Interfacial Electrochem. **150**, 19 (1983).

[40] J. Huang, Y. Zhang, M. Li, A. Groß, and S. Sakong, Comparing ab initio molecular dynamics and a semiclassical grand canonical scheme for the electric double layer of the Pt(111)/water interface, J. Phys. Chem. Lett. **14**, 2354 (2023).

[41] J. Le, M. Iannuzzi, A. Cuesta, and J. Cheng, Determining potentials of zero charge of metal electrodes versus the standard hydrogen electrode from density-functional-theory-based molecular dynamics, Phys. Rev. Lett. **119**, 016801 (2017).

[42] L. Li, Y.-P. Liu, J.-B. Le, and J. Cheng, Unraveling molecular structures and ion effects of electric double layers at metal water interfaces, Cell Rep. Phys. Sci. **3**, 100759 (2022).

[43] R. Blossey and R. Podgornik, Continuum theories of structured dielectrics, Europhys. Lett. **139**, 2 (2022).

[44] G. Monet, F. Bresme, A. Kornyshev, and H. Berthoumieux, Nonlocal dielectric response of water in nanoconfinement, Phys. Rev. Lett. **126**, 21 (2021).

[45] M. Vatin, A. Porro, N. Sator, J.-F. Dufrêche, and H. Berthoumieux, Electrostatic interactions in water: A nonlocal electrostatic approach, Mol. Phys. **119**, e1825849 (2021).

[46] J. G. Hedley, H. Berthoumieux, and A. A. Kornyshev, The dramatic effect of water structure on hydration forces and the electrical double layer, J. Phys. Chem. C **127**, 18 (2023).

[47] R. Blossey and R. Podgornik, Field theory of structured liquid dielectrics, Phys. Rev. Res. **4**, 2 (2022).

[48] R. Blossey and R. Podgornik, A comprehensive continuum theory of structured liquids, J. Phys. A:Math. Theor. **56**, 2 (2023).

[49] S. Hagiwara, S. Nishihara, F. Kuroda, and M. Otani, Development of a dielectrically consistent reference interaction site model combined with the density functional theory for electrochemical interface simulations, Phys. Rev. Mater. **6**, 093802 (2022).

[50] N. Bruch, T. Binninger, J. Huang, and M. Eikerling, Incorporating electrolyte correlation effects into variational models of electrochemical interfaces, J. Phys. Chem. Lett. **15**, 2015 (2024).

[51] A. Kasina, E. Cocklin, S. Horswell, Y. Grunder, and C. A. Lucas, Structure of the electrochemical interface: Ag(*hkl*) in an alkaline electrolyte, J. Phys. Chem. C **128**, 13318 (2024).

[52] M. S. Shibata, Y. Morimoto, I. V. Zenyuk, and A. Z. Weber, Parameter-fitting-free continuum modeling of electric double layer in aqueous electrolyte, J. Chem. Theory Comput. **20**, 6184 (2024).

[53] K. Letchworth-Weaver and T. A. Arias, Joint density functional theory of the electrode-electrolyte interface: Application to fixed electrode potentials, interfacial capacitances, and potentials of zero charge, Phys. Rev. B **86**, 075140 (2012).

[54] R. Jinnouchi and A. B. Anderson, Electronic structure calculations of liquid-solid interfaces: Combination of density functional theory and modified Poisson-Boltzmann theory, Phys. Rev. B **77**, 245417 (2008).

[55] S. Nishihara and M. Otani, Hybrid solvation models for bulk, interface, and membrane: Reference interaction site methods coupled with density functional theory, Phys. Rev. B **96**, 115429 (2017).

[56] N. Abidi and S. N. Steinmann, An electrostatically embedded QM/MM scheme for electrified interfaces, ACS Appl. Mater. Interfaces **15**, 25009 (2023).

[57] N. Di Pasquale, A. R. Finney, J. D. Elliott, P. Carbone, and M. Salvalaglio, Constant chemical potential–quantum mechanical–molecular dynamics simulations of the graphene–electrolyte double layer, J. Chem. Phys. **158**, 134714 (2023).

[58] J. Huang, Density-potential functional theory of electrochemical double layers: Calibration on the Ag (111)-KPF_6 system and parametric analysis, J. Chem. Theory Comput. **19**, 3 (2023).

[59] J. Huang, Hybrid density-potential functional theory of electric double layers, Electrochim. Acta **389**, 138720 (2021).

[60] S. Lundqvist and N. H. March, *Theory of the Inhomogeneous Electron Gas* (Springer Science & Business Media, New York, 2013).

[61] L. H. Thomas, The calculation of atomic fields, Math. Proc. Cambridge Philos. Soc. **23**, 542 (1927).

[62] E. Fermi, Eine statistische Methode zur Bestimmung einiger Eigenschaften des Atoms und ihre Anwendung auf die Theorie des periodischen Systems der Elemente, Z. Für Phys. **48**, 73 (1928).

[63] J. P. Perdew and S. Kurth, in *A Primer in Density Functional Theory*, edited by C. Fiolhais, F. Nogueira, and M. A. L. Marques (Springer, Berlin, Heidelberg, 2003), pp. 1–55.

[64] J. P. Perdew, K. Burke, and M. Ernzerhof, Generalized gradient approximation made simple, Phys. Rev. Lett. **77**, 3865 (1996).

[65] Valentin V. Karasiev, Lázaro Calderín, and S. B. Trickey, Importance of finite-temperature exchange correlation for warm dense matter calculations, Phys. Rev. E **93**, 063207 (2016).

[66] R. Podgornik, Theory of inhomogeneous rod-like Coulomb fluids, Symmetry **13**, 2 (2021).

[67] J.-M. Caillol, O. Patsahan, and I. Mryglod, Statistical field theory for simple fluids: The collective variables representation, Phys. A **368**, 2 (2006).

[68] Y. A. Budkov and A. L. Kolesnikov, Modified Poisson–Boltzmann equations and macroscopic forces in inhomogeneous ionic fluids, J. Stat. Mech.:Theory Exp. **2022**, 053205 (2022).

[69] L. Lue, A variational field theory for solutions of charged, rigid particles, Fluid Phase Equilib. **241**, 236 (2006).

[70] E. Wicke and M. Eigen, Über den Einfluß des Raumbedarfs von Ionen in wäßriger Lösung auf ihre Verteilung in elektrischen Feld und ihre Aktivitätskoeffizienten, Z. Für Elektrochem. Berichte Bunsenges. Für Phys. Chem. **56**, 551 (1952).

[71] M. Eigen and E. Wicke, The thermodynamics of electrolytes at higher concentration, J. Phys. Chem. **58**, 702 (1954).

[72] V. Freise, Zur Theorie der diffusen Doppelschicht, Z. Für Elektrochem. Berichte Bunsenges. Für Phys. Chem. **56**, 822 (1952).

[73] J. Huang, S. Chen, and M. Eikerling, Grand-canonical model of electrochemical double layers from a hybrid density–potential functional, J. Chem. Theory Comput. **17**, 4 (2021).

[74] J. Huang, F. Domínguez-Flores, and M. Melander, Variants of surface charges and capacitances in electrocatalysis: Insights from density-potential functional theory embedded with an implicit chemisorption model, PRX Energy **3**, 043008 (2024).

[75] M. M. Melander, T. Wu, T. Weckman, and K. Honkala, Constant inner potential DFT for modelling electrochemical systems under constant potential and bias, Npj Comput. Mater. **10**, 5 (2024).

[76] See Supplemental Material at http://link.aps.org/supplemental/10.1103/PhysRevApplied.23.024009 for supplementary figures and technical details on the numerical implementation.

[77] L. A. Constantin, E. Fabiano, and F. Della Sala, Nonlocal kinetic energy functional from the jellium-with-gap

model: Applications to orbital-free density functional theory, Phys. Rev. B **97**, 205137 (2018).
[78] C. N. Rowley and B. Roux, The solvation structure of Na^+ and K^+ in liquid water determined from high level *ab initio* molecular dynamics simulations, J. Chem. Theory Comput. **8**, 3526 (2012).
[79] S. G. Raju and S. Balasubramanian, Aqueous solution of [bmim][PF_6]: Ion and solvent effects on structure and dynamics, J. Phys. Chem. B **113**, 4799 (2009).
[80] K. Amann-Winkel, M.-C. Bellissent-Funel, L. E. Bove, T. Loerting, A. Nilsson, A. Paciaroni, D. Schlesinger, and L. Skinner, X-ray and neutron scattering of water, Chem. Rev. **116**, 7570 (2016).
[81] A. M. Kuznetsov and J. Ulstrup, in *Electron Transfer in Chemistry and Biology: An Introduction to the Theory* (John Wiley & Sons Ltd, Chichester, UK, 1999).
[82] N. Bruch, M. Eikerling, and J. Huang, Density-Potential Functional Theory of Metal-Solution Interfaces, (2023).
[83] H. U. Yang, J. D'Archangel, M. L. Sundheimer, E. Tucker, G. D. Boreman, and M. B. Raschke, Optical dielectric function of silver, Phys. Rev. B **91**, 235137 (2015).
[84] E. Gongadze and A. Iglič, Decrease of permittivity of an electrolyte solution near a charged surface due to saturation and excluded volume effects, Bioelectrochemistry **87**, 199 (2012).
[85] J. Ulstrup, in *Charge Transfer Processes in Condensed Media*, edited by J. Ulstrup (Springer, Berlin, Heidelberg, 1979), pp. 40–70.
[86] W. Tang, S. Zhao, and J. Huang, Origin of solvent dependency of the potential of zero charge, JACS Au **3**, 3381 (2023).
[87] J. Cheng and M. Sprik, Alignment of electronic energy levels at electrochemical interfaces, Phys. Chem. Chem. Phys. **14**, 11245 (2012).
[88] L. Andersson and C. Zhang, Molecular dynamics simulations of metal-electrolyte interfaces under potential control, Curr. Opin. Electrochem. **42**, 101407 (2023).
[89] M. F. Toney, J. N. Howard, J. Richer, G. L. Borges, J. G. Gordon, O. R. Melroy, D. G. Wiesler, D. Yee, and L. B. Sorensen, Voltage-dependent ordering of water molecules at an electrode–electrolyte interface, Nature **368**, 444 (1994).
[90] J. Le, A. Cuesta, and J. Cheng, The structure of metal-water interface at the potential of zero charge from density functional theory-based molecular dynamics, J. Electroanal. Chem. **819**, 87 (2018).
[91] S. Schnur and A. Groß, Properties of metal–water interfaces studied from first principles, New J. Phys. **11**, 12 (2009).
[92] A. Roudgar and A. Groß, Water bilayer on the Pd/Au(111) overlayer system: Coadsorption and electric field effects, Chem. Phys. Lett. **409**, 157 (2005).
[93] J.-J. Velasco-Velez, C. H. Wu, T. A. Pascal, L. F. Wan, J. Guo, D. Prendergast, and M. Salmeron, The structure of interfacial water on gold electrodes studied by x-ray absorption spectroscopy, Science **346**, 831 (2014).
[94] Y. Tong, F. Lapointe, M. Thämer, M. Wolf, and R. K. Campen, Hydrophobic water probed experimentally at the gold electrode/aqueous interface, Angew. Chem. Int. Ed. **56**, 4211 (2017).
[95] N. García-Aráez, V. Climent, and J. M. Feliu, Evidence of water reorientation on model electrocatalytic surfaces from nanosecond-laser-pulsed experiments, J. Am. Chem. Soc. **130**, 3824 (2008).
[96] J. M. Yoo, J. Ingenmey, M. Salanne, and M. R. Lukatskaya, Anion effect in electrochemical CO_2 reduction: From spectators to orchestrators.
[97] M. Koper, Theory and kinetic modeling of electrochemical cation-coupled electron transfer reactions, J. Solid State Electrochem. **1**, 1601 (2023).
[98] X. Qin, H. A. Hansen, K. Honkala, and M. M. Melander, Cation-induced changes in the inner- and outer-sphere mechanisms of electrocatalytic CO_2 reduction, Nat. Commun. **14**, 7607 (2023).
[99] S. Ringe, C. G. Morales-Guio, L. D. Chen, M. Fields, T. F. Jaramillo, C. Hahn, and K. Chan, Double layer charging driven carbon dioxide adsorption limits the rate of electrochemical carbon dioxide reduction on gold, Nat. Commun. **11**, 1 (2020).
[100] W. Schmickler, Double layer theory, J. Solid State Electrochem. **24**, 2175 (2020).
[101] J. Huang, J. Zhang, and M. Eikerling, Unifying theoretical framework for deciphering the oxygen reduction reaction on platinum, Phys. Chem. Chem. Phys. **20**, 11776 (2018).
[102] L. Zhang, J. Cai, Y. Chen, and J. Huang, Modelling electrocatalytic reactions with a concerted treatment of multistep electron transfer kinetics and local reaction conditions, J. Phys.:Condens. Matter **33**, 504002 (2021).
[103] S. Ringe, E. L. Clark, J. Resasco, A. Walton, B. Seger, A. T. Bell, and K. Chan, Understanding cation effects in electrochemical CO_2 reduction, Energy Environ. Sci. **12**, 3001 (2019).
[104] L. B. T. de Kam, T. L. Maier, and K. Krischer, Electrolyte effects on the alkaline hydrogen evolution reaction: A mean-field approach, (2024).
[105] W. Schmickler and R. Guidelli, The partial charge transfer, Electrochim. Acta **127**, 489 (2014).
[106] S. Trasatti, Work function, electronegativity, and electrochemical behaviour of metals, J. Electroanal. Chem. Interfacial Electrochem. **33**, 351 (1971).
[107] S. Trasatti, in *Trends in Interfacial Electrochemistry*, edited by A. F. Silva (Springer Netherlands, Dordrecht, 1986), pp. 25–48.
[108] M. Z. Bazant, M. S. Kilic, B. D. Storey, and A. Ajdari, Towards an understanding of induced-charge electrokinetics at large applied voltages in concentrated solutions, Adv. Colloid Interface Sci. **152**, 1 (2009).
[109] P. Li, J. Huang, Y. Hu, and S. Chen, Establishment of the potential of zero charge of metals in aqueous solutions: Different faces of water revealed by ab initio molecular dynamics simulations, J. Phys. Chem. C **125**, 3972 (2021).
[110] A. Iglič, E. Gongadze, and K. Bohinc, Excluded volume effect and orientational ordering near charged surface in solution of ions and Langevin dipoles, Bioelectrochemistry **79**, 223 (2010).
[111] A. S. Shatla, M. Landstorfer, and H. Baltruschat, On the differential capacitance and potential of zero charge of Au(111) in some aprotic solvents, ChemElectroChem **8**, 1817 (2021).